

A 40-BILLION SOLAR MASS BLACK HOLE IN THE EXTREME CORE OF HOLM 15A,  
THE CENTRAL GALAXY OF ABELL 85

KIANUSCH MEHRGAN,<sup>1,2</sup> JENS THOMAS,<sup>1,2</sup> ROBERTO SAGLIA,<sup>1,2</sup> XIMENA MAZZALAY,<sup>1,2</sup> PETER ERWIN,<sup>1,2</sup>  
RALF BENDER,<sup>1,2</sup> MATTHIAS KLUGE,<sup>1,2</sup> AND MAXIMILIAN FABRICIUS<sup>1,2</sup>

<sup>1</sup>*Max-Planck-Institut für extraterrestrische Physik, Giessenbachstrasse, D-85748 Garching*

<sup>2</sup>*Universitäts-Sternwarte München, Scheinerstrasse 1, D-81679 München, Germany*

Submitted to ApJ

ABSTRACT

Holm 15A, the brightest cluster galaxy (BCG) of the cool-core cluster Abell 85, has an ultra-diffuse central region,  $\sim 2$  mag fainter than the faintest depleted core of any early-type galaxy (ETG) that has been dynamically modelled in detail. New photometric data taken at the Wendelstein observatory confirm the previously noted unusual, near-exponential light profile of the galaxy's core. We use orbit-based, axisymmetric Schwarzschild models to analyse the stellar kinematics of Holm 15A from new high-resolution, wide-field spectral observations obtained with MUSE at the VLT. We find a supermassive black hole (SMBH) with a mass of  $(4.0 \pm 0.80) \times 10^{10} M_{\odot}$  at the center of Holm 15A. This is the most massive black hole with a direct dynamical detection in the local universe. We find that the distribution of stellar orbits is increasingly biased towards tangential motions inside the core. However, the tangential bias is less than in other cored elliptical galaxies. We compare Holm 15A with N-body simulations of mergers between galaxies with black holes and find that the observed amount of tangential anisotropy and the shape of the light profile are consistent with a formation scenario where Holm 15A is the remnant of a merger between two ETGs with pre-existing depleted cores. We find that black hole masses in cored galaxies, including Holm 15A, scale inversely with the central stellar surface brightness and mass density, respectively. These correlations are independent of a specific parameterization of the light profile.

*Keywords:* galaxies: supermassive black holes – galaxies: ETG and lenticular, cD – galaxies: evolution – galaxies: formation – stars: kinematics and dynamics – galaxies: center – clusters: individual (Abell 85)

1. INTRODUCTION

Holm 15A, the brightest cluster galaxy of Abell 85, is a massive,  $M_{\star} \gtrsim 2 \times 10^{12} M_{\odot}$  early-type galaxy (ETG) with a nearly exponential central surface brightness profile (Sérsic index  $n \sim 1$ , (Bonfini et al. 2015; Madrid & Donzelli 2016)). Holm 15A has little angular momentum, its rotational velocity  $v_{rot} \lesssim 40$  km/s is small compared to the velocity dispersion  $\sigma \sim 350$  km/s. This is very common among massive ETGs (e.g. Emsellem et al. 2011; Cappellari 2016; Veale et al. 2017). The light profile of the galaxy exhibits a very diffuse low-surface-brightness center. This is not surprising either since diffuse centers

are also common among massive elliptical galaxies (e.g. Faber et al. 1997; Lauer et al. 2007a). What is striking about Holm 15A is *how large* and *how faint* the central diffuse region of the galaxy is. Among the 88 core galaxies in the Lauer et al. (2007a) sample, the faintest core is still  $\sim 0.5$  mag/arcsec<sup>2</sup> brighter than the center of Holm 15A. Among galaxies with detailed dynamical models, the difference is even larger:  $\sim 2$  mag/arcsec<sup>2</sup> (Rusli et al. 2013b, Thomas et al. 2016, cf. Figure 1).

In addition to having an extremely faint core, Holm 15A differs from other massive elliptical galaxies in another, more subtle aspect of its light profile that we will discuss in the following.

Diffuse, shallow central surface brightness regions have been observed in massive ETGs for a long time (e.g. Lauer 1985; Kormendy 1985; Faber et al. 1987),

arXiv:1907.10608v1 [astro-ph.GA] 24 Jul 2019

but it was only after the advent of the *Hubble Space Telescope (HST)* that they could be properly resolved (e.g. Ferrarese et al. 1994; Lauer et al. 1995, hereafter L+95). In order to quantitatively assess the centers of ETGs observed with HST, first a broken power-law profile was used, the so-called ‘Nuker profile’ (Lauer et al. 1995). Lauer et al. (1995) classified galaxies as having ‘cores’ when the light profile shows a clear break with a shallow power-law slope  $\gamma$  inside the break radius  $r_b$ :  $0 \lesssim \gamma \lesssim 0.3$ .

Graham et al. (2003) and Trujillo et al. (2004) introduced the core-Sérsic profile as an alternative parametric description for ETGs. The inner parts of the core-Sérsic profile, interior to the break (or “core”) radius, describe again a power-law surface brightness distribution. In the outer parts, however, the profile turns into a Sérsic function rather than into another power-law. This makes the core-Sérsic profile suitable to fit ETGs out to larger radii. Nuker break radii and core-Sérsic core radii are in most cases similar and denote the central region of cored ETGs where both the surface brightness is low and the slope of the surface brightness profile is shallow. In core ellipticals the Sérsic index is generally high,  $n \gtrsim 4$ . This is the second distinct feature of Holm 15A: the central light profile of the galaxy is almost exponential (Sérsic index  $n \sim 1$ ).

The obvious question is whether the distinct properties of the core in Holm 15A – (1) its extreme faintness and (2) its almost exponential light profile – imply an alternative formation channel for cores in massive galaxies or whether it is a core that simply probes the rare extremes of the distribution of “classical” core properties.

The contemporary view of the formation of cores in massive ETGs is that the observed properties of cores are best explained via so-called black hole binary ‘core scouring’. Core scouring is driven by the hardening of a SMBH binary naturally formed during dissipationless mergers between ETGs which are thought to dominate the late growth processes of massive galaxies (e.g. Khochfar & Burkert 2003; Naab et al. 2006; Boylan-Kolchin et al. 2006; De Lucia et al. 2006; Oser et al. 2010). Gravitational slingshots eject stars on predominantly radial orbits from the center of the remnant galaxy, producing a cored central light profile (e.g. Begelman et al. 1980; Hills & Fullerton 1980; Ebisuzaki et al. 1991; Trujillo et al. 2004; Milosavljević & Merritt 2001; Volonteri et al. 2003; Merritt & Milosavljević 2005; Merritt 2006a, 2013; Rusli et al. 2013a; Rantala et al. 2018). This core-formation channel can explain the fundamental characteristics of core galaxies: (1) the observed uniform tangentially biased orbit structure in

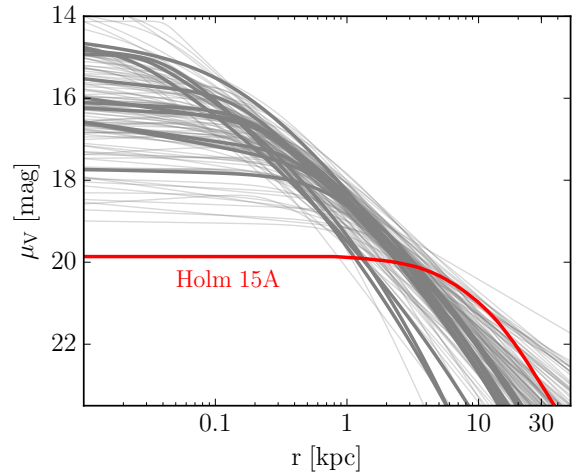


**Figure 1.** V-Band surface brightness profile of Holm 15A compared to Nuker models of cored ETGs from Lauer et al. (2007a) (light gray) and core-Sérsic models of cored ETGs with SMBH detections from Rusli et al. (2013a) and Thomas et al. (2016) (dark gray). Holm 15A’s light profile has been shifted from g-band assuming  $g-V = 0.14$  (Fukugita et al. 1995), a K correction of 0.13, cosmological dimming of 0.23 and a galactic extinction of  $A_g = 0.125$ .

cores (Milosavljević & Merritt 2001; Thomas et al. 2014; Rantala et al. 2018) and (2) the various core-specific scaling relations between the black hole mass, core size, size of the gravitational sphere of influence and ‘missing’ light compared to the inwards extrapolation of the steeper outer light profile (from which the core ‘breaks’; Lauer et al. 2007b; Kormendy & Bender 2009; Kormendy & Ho 2013; Thomas et al. 2016; Rantala et al. 2018). In particular, since larger black holes produce larger and fainter cores, the most massive ETGs are expected to exhibit the most extended and diffuse central surface brightness profiles (Faber et al. 1997; Lauer et al. 2007a; Rusli et al. 2013a).

The size of the core in Holm 15A is difficult to determine. As stated before, the central light profile of Holm 15A is almost exponential. Hence, while the logarithmic slope of the central light profile in Holm 15A is still small (in the same range as the power-law slopes of core galaxies, cf. Figure 1), Holm 15A lacks a clear break radius and the slope continues to change down to the smallest observed radii. In order to characterize the size of the central region where the surface brightness is low and where the slope of the surface brightness profile is shallow, López-Cruz et al. (2014) used the cusp radius  $r_\gamma$  derived from a Nuker-profile fit, which is defined as the radius where the logarithmic slope  $\gamma$  of the surface-brightness profile equals  $-0.5$ . Their cusp radius is  $r_\gamma = 4.57 \pm 0.06$  kpc (López-Cruz et al. 2014), larger than any previously known core (cf. e.g. Post-

man et al. 2012; Rusli et al. 2013a). A core galaxy with such a large core radius would be expected to host a SMBH with  $M_{BH} \sim 10^{11} M_{\odot}$ , based on  $M_{BH} - r_{\gamma}$  scaling relations from Lauer et al. (2007c) and Thomas et al. (2016).

Feedback from an active galactic nucleus (AGN) has been suggested as a mechanism for the formation of cores as well (e.g. Martizzi et al. 2012; Choi et al. 2018). If the different light profile of Holm 15A indeed results from a different formation mechanism then the galaxy may not follow the core-specific black-hole scaling relations that are typical for core galaxies. For example, a coreless galaxy with the same velocity dispersion and stellar mass as Holm 15A would be expected to host a black hole of only  $\sim 3 \times 10^9 M_{\odot}$  (using  $M_{BH} - \sigma$ ,  $M_{Bu}$  scaling relations for core-less ETGs from McConnell & Ma 2013; Saglia et al. 2016), almost two order of magnitude lower than the black hole mass implied by the core. The galaxy might also not show the specific tangential orbit composition that characterises other core galaxies. Hence, determining the black hole mass and orbital structure of Holm 15A is critical for understanding how the galaxy formed.

In this paper we use dynamical models based on new spectroscopic observations with the MUSE IFU<sup>1</sup> to investigate in detail the internal orbital structure and mass composition of Holm 15A. The goal is to shed light on the unresolved issues related to its formation and evolution: Is the center of Holm 15A an extreme version of a depleted galaxy core, just gradually different from less extreme cores? Or has the core of Holm 15A formed via a completely different mechanism, e.g. extreme AGN feedback?

This paper is structured as follows: Section 2 describes in detail the photometric properties of Holm 15A's unusual light profile using new *i*-band photometry of Holm 15A obtained with the Fraunhofer Telescope at the Wendelstein Observatory and MUSE spectroscopy. Section 3 details the spectroscopic and kinematic data used in this study. The dynamical models and results are presented in Section 4. In Section 5 we discuss these results and their implications, in particular in view of predictions from N-body simulations. We summarize our conclusions about Holm 15A in section 6.

We use the Planck  $\Lambda$ CDM (Planck Collaboration et al. 2018) cosmological model,  $H_0 = 67.4$ ,  $\Omega_M = 0.315$ . The redshift of Holm 15A,  $z = 0.055$ , then corresponds to a

luminosity distance of  $D_L = 252.8$  Mpc and an angular diameter distance of  $D_A = 227.2$  Mpc ( $1'' = 1.10$  kpc).

## 2. PHOTOMETRY

We used two image sources for our photometric and morphological analysis of Holm 15A. The first is an *i*-band image obtained with the Fraunhofer Telescope at the Wendelstein observatory using the Wendelstein Wide Field Imager (WWFI, Kosyra et al. 2014). A detailed description of the observations and data reduction will be published in Kluge et al. in prep. While a *g*-band image was also available, the *i*-band image had significantly better seeing (Moffat FWHM from fits to multiple stars =  $0''.86$  versus  $1''.8$  for the *g*-band image). The field-of-view (FOV) of this observation, centered on Holm 15A covers  $49' \times 52'$  (pixel size  $0''.4/\text{pixel}$ ), corresponding to roughly  $10$  (Mpc)<sup>2</sup>.

We used this image for the isophote analysis on which the 3D deprojection is based that we use to constrain the dynamical models. We also used this image to attempt different determinations of the size of the core in Holm 15A (Sec. 2.1) which is important for the discussion later on (cf. Sec. 5).

The second source is the MUSE data cube which we also used to obtain 2D stellar kinematics (see section 3.2 for a detailed description, including observation and data reduction). Here, in Section 2.2, however, we use it to analyse Holm 15A for the presence of dust structure or color gradients which could potentially bias the deprojection.

### 2.1. Analysis of the Wendelstein image: Holm 15A's exponential light profile and core size

Comparing the distribution of stars in Holm 15A to those of other cored ETGs (cf. Figure 1) it is clear that Holm 15A is not only characterised by an extreme *deficit* of light in the inner core but also by an *excess* of light adjacent to the core out to roughly  $20''$  (or  $\sim 20$  kpc, respectively).

Ellipse fits to the Wendelstein image using the IRAF task *ellipse* (Carter 1978; Jędrzejewski 1987) yield a surface brightness profile and isophote shape measurements that can be traced to at least  $250''$  (see Figure 2). We also performed 2D fits to the *i*-band image using IMFIT (Erwin 2015). Our goal in performing these fits was to better understand the structure of the unusual core-light profile of Holm 15A. In particular, we were interested in finding a robust estimate of the size of the core in Holm 15A. For the generation of the 3D luminosity distribution (cf. Sec. 2.3), we use the surface brightness profile from the ellipse fits.

Beyond about  $140''$ , the position angle twists by about  $90^\circ$ , and the ellipticity drops from  $\sim 0.4$  to  $\sim 0.2$  (see

<sup>1</sup> Based on observations collected at the European Organisation for Astronomical Research in the Southern Hemisphere under ESO program 099.B-0193(A).

Figure 2). Meanwhile, the centers of the fitted ellipses begin varying by as much as  $\sim 15''$ . It is not clear how much of this represents a real change in the isophotes, e.g. if this is related to a transition to intra-cluster light, or how much is simply an artifact of the increasingly low S/N (signal-to-noise ratio). We therefore confine our 2D fitting to  $a < 140''$ . In addition to masking stars and galaxies overlapping with the main body of Holm 15A, we masked out everything outside an ellipse with  $a = 130''$ , ellipticity = 0.4, and the same orientation as the main galaxy. We convolved the model images using a Moffat-function PSF image based on the median characteristics of 19 stars in the image, FWHM =  $0''.86$ .

We find that fitting the image with an inner Sérsic function that is near-exponential in shape, with a Sérsic index of  $n = 0.99$ , and an outer Sérsic component with  $n = 1.48$  results in a good fit to the Wendelstein data. This is broadly consistent with the previous 2D analysis of a CFHT  $r$ -band image by Bonfini et al. (2015).

Following previous studies on quantifying core properties, we experimented with replacing the inner, exponential-like Sérsic component with a core-Sérsic component (Graham et al. 2003; Trujillo et al. 2004), which resulted in a slightly better fit. Nonetheless, there was still a distinct, bilobed excess in the residual image from the core-Sérsic + Sérsic fit, on a scale of  $a \sim 4''$ . Therefore we experimented with adding additional components to the model. The best result was with the GaussianRing3D function of IMFIT, which performs line-of-sight integration for an inclined ring with a Gaussian radial density and an exponential vertical density. The final result was a fit with central residuals which were almost completely lacking in any systematics (see Figure 3).

The “ring” component has a semi-major axis of  $4''.1$ , a position angle of  $53^\circ$  – almost perpendicular to the Sérsic components – and is intrinsically circular, viewed at an inclination of  $68^\circ$ . We emphasize that this is a purely empirically chosen function which produces approximately the right excess light to minimize the residuals; it is not necessarily evidence for an actual inclined ring. We also note that this may be consistent with the extra Gaussian-like Sérsic component (with  $n = 0.3$ ) – with a position angle of  $\sim 55^\circ$  – which Bonfini et al. (2015) added to their 2D fits as a “corrective” component.

The best-fit parameters of this model are listed in Table 1. The core-related parameters of interest are the break radius  $r_b$ , which is  $2''.6 \pm 0''.05$  ( $2.8 \pm 0.06$  kpc), and the inner logarithmic slope,  $\gamma \approx 0.10$ . The value of  $r_b$  is quite robust and varies by only 5% when fitting with or without the ring-component. The break

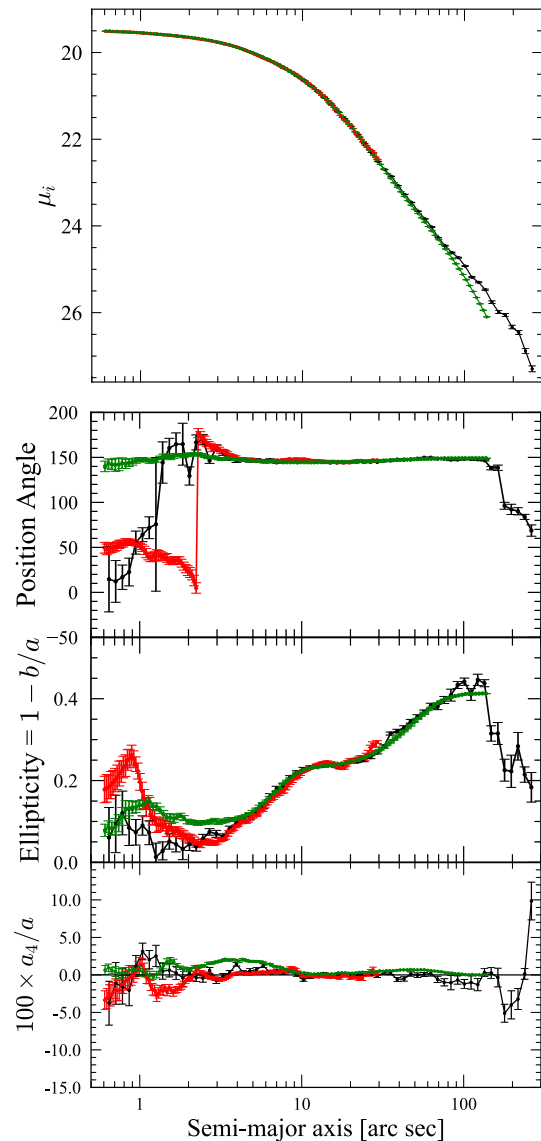


**Figure 2.** Ellipse fits to the isophotes of Holm 15A for our  $i$ -band Wendelstein image (black), the red image extracted from our MUSE data cube (red), and the best-fitting 2D model image (green). From top to bottom, the panels show  $i$ -band surface brightness, position angle, ellipticity,  $a_4/a = \sqrt{b/a} * \cos 4\theta$  parameter versus semi-major axis on a logarithmic scale.

radius is smaller than the circularised cusp radius  $r_\gamma = 3''.7 \pm 0''.10$  ( $4.1 \pm 0.11$  kpc) that we measure directly from the logarithmic derivative of the ellipse-fit surface-brightness profile (the semi-major axis length of the corresponding isophote is  $r_\gamma = 4''.1 \pm 0''.10$ , consistent with previous measurements, e.g. López-Cruz et al. 2014). We will discuss the light profile and the difference between break and cusp radius further in Sec. 5.2.

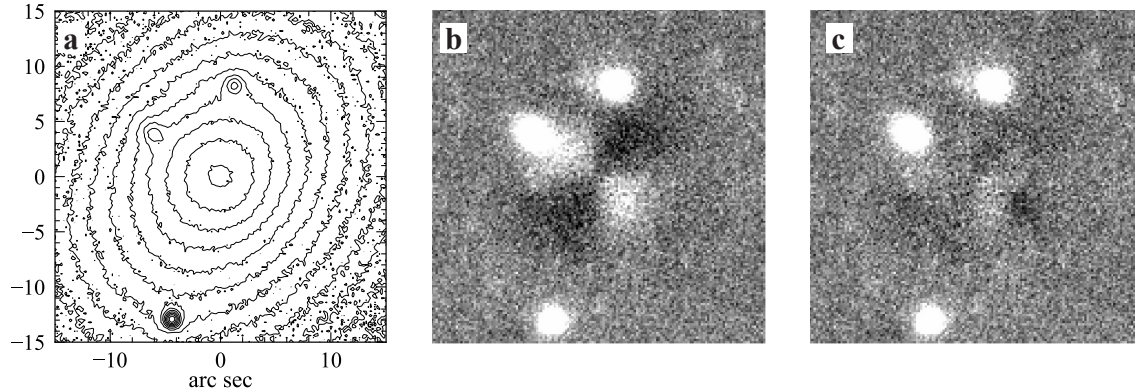


**Figure 3.** Data and residuals for 2D fits. **a:** Inner isophotes for Wendelstein  $i$ -band image of Holm 15A; peak galaxy intensity is  $\approx 700$  counts/pixel. **b:** Residuals for the core-Sérsic + Sérsic model (data – model), plotted on a linear scale from  $-25$  (black) to  $+25$  (white) counts/pixel. **c:** Same as for panel b, but for the core-Sérsic + Sérsic + GaussianRing3D model.

The core parameters we measure are rather different from those found by Bonfini et al. (2015) in their core-Sérsic + Sérsic fits (e.g.,  $r_b \approx 0''.7$ ). This may have to do with the fact that our fits include more of the galaxy (theirs only extended out to about  $a = 90''$ ) and that our outer component is a second Sérsic function rather than the exponential function that Bonfini et al. (2015) used.

### 2.2. MUSE images: no evidence for dust or color gradients

To investigate whether dust extinction might distort the isophotes, and to check for color gradients indicative of a change in the stellar populations, we also generated images from the MUSE data cube. This has two advantages. First, the MUSE observations have (slightly) better seeing than the Wendelstein  $i$ -band image: in the “red” image (see below for definition), we measured  $\text{FWHM} = 0''.72$  from the two point sources in the image. Second, when collapsing the data cube we can choose wavelength ranges that explicitly exclude emission, which is important because we do detect regions of line emission within Holm 15A (see below).

Ellipse fits to an image extracted from a red, emission-line-free subset of the data cube (using 7300–8500 Å) are shown in Figure 2 in red; they agree well with the Wendelstein  $i$ -band ellipse fits, except that the ellipticities in the very center ( $a \leq 1''$ ) are somewhat higher for the MUSE image, consistent with its better seeing.

In addition to the red image mentioned above, we used the spectral region 4750–5500 Å to create a largely emission-line-free “blue” image. The ratio of the blue and red MUSE images is shown in the right-hand panel of Figure 4 and it shows *no* evidence for either dust lanes or significant color gradients.

### 2.3. 3D deprojection

Component	Parameter	Value	units
Core-Sérsic	PA	$141.9 \pm 0.2$	deg
	$\epsilon$	$0.187 \pm 0.002$	
	$n$	$0.965 \pm 0.005$	
	$I_b$	$20.040 \pm 0.012$	mag arcsec $^{-2}$
	$r_e$	$12.87 \pm 0.04$	arc sec
	$r_b$	$2.57 \pm 0.05$	arc sec
	$\alpha$	$12.15 \pm 4.1$	
Sérsic	PA	$149.0 \pm 0.1$	deg
	$\epsilon$	$0.413 \pm 0.003$	
	$n$	$1.69 \pm 0.03$	
	$I_e$	$24.035 \pm 0.016$	mag arcsec $^{-2}$
	$r_e$	$60.67 \pm 0.48$	arc sec
GaussianRing3D	PA	$52.1 \pm 0.9$	deg
	inclination	$81.8 \pm 1.5$	deg
	$J_0$	$1.08 \pm 0.03$	counts pixel $^{-3}$
	$a$	$4.37 \pm 0.07$	arc sec
	$\sigma$	$1.76 \pm 0.05$	arc sec
	$h_z$	$2.78 \pm 0.10$	arc sec

**Table 1.** Best-fit IMFIT model for the  $i$ -band image of Holm 15A. Column 1: component used in fit. Column 2: parameter. Column 3: best-fit value for parameter and  $1 - \sigma$  confidence limits from 200 rounds of bootstrap resampling. Column 4: units. Note that for the GaussianRing3D component, we fixed the ring PA and ellipticity to both be zero, so these are not listed in the table.

In order to constrain the distribution of stars in our dynamical model of Holm 15A (see Section 4), we create a 3D deprojection of the luminosity density from our deconvolved 2D Wendelstein image. The algorithm that we use to achieve this enables us to find a 3D non-parametric axisymmetric luminosity density distribution  $\nu(\mathbf{r})$  consistent with the 2D input surface bright-

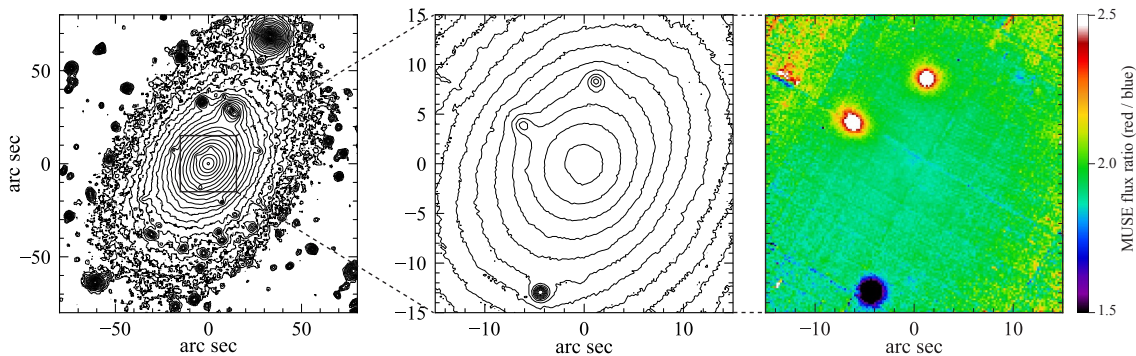


**Figure 4.** Holm 15A isophotes and central color map. Left: Logarithmically scaled isophotes for our Wendelstein  $i$ -band image (median-smoothed with an 11-pixel-wide box). Middle: Isophotes for the MUSE red image (extracted from data cube using 7300–8500 Å). Right: Color map from ratio of MUSE blue (4750–5500 Å) and red images. No evidence for dust lanes or a color gradient in the central region of the galaxy can be seen.

ness distribution and an assumed inclination angle  $i$ . As can be seen in Figure 2, Holm 15A is for the most part relatively round, but flattens significantly to an ellipticity  $\varepsilon \sim 0.4$  at the largest radius of our best-fit 2D model image. In the axisymmetric case, this limits possible viewing angles to angles close to edge on, which is why we assume  $i = 90^\circ$  and thus that our deprojection is unique. The algorithm utilizes a penalized log-likelihood function and is detailed in Magorrian (1999).

As Figure 2 shows, the position angle of the galaxy is remarkably stable from  $3''$  out to at least  $100''$ , suggesting that Holm 15A might be close to rotational symmetry. Towards the very center, the isophotes start rotating but at the same time the galaxy becomes significantly rounder. For example, our best-fit 3-component decomposition formally produces isophotes with a position angle that is rotated by nearly  $90^\circ$  with respect to the observations inside  $3''$ . However, because that region of the core is close to circular, the *actual* residuals between this model and the observed image are small (Figure 3). An axisymmetric luminosity density distribution can reproduce the relevant observed photometric features similarly well.

### 3. MUSE SPECTROSCOPY: STELLAR KINEMATICS OF HOLM 15A

#### 3.1. MUSE observations and data reduction

We obtained wide-field spectroscopic data of Holm 15A from the Multi-Unit Spectroscopic Explorer (MUSE) at the *Very Large Telescope* at Paranal on 2017 November 16 and 2018 August 10. At  $z = 0.055$  MUSE covers several important absorption features such as  $H\beta$ , the Mgb region, NaI, several Fe absorption features and the Ca II triplet.

Our observations were carried out over the course of two nights and consist of three observational blocks of two dithered 1200s exposures of Holm 15A plus one

300s-long exposure of the sky, inbetween each. All observations, including the sky-field offset, cover an approximately  $1' \times 1'$  FOV composed of 24 combined integral field units (IFUs).

We performed the data reduction using version 2.8.5 of the standard Esoreflex MUSE pipeline supplied by ESO (Freudling et al. 2013). The pipeline runs several recipes on both exposures such as flat-field and wavelength calibrations and returns a combined data cube, covering the optical domain from about 4800 Å to 9400 Å with a spectral resolution of 1.25 Å. We sampled the cube in spaxels of  $0''.4 \times 0''.4$ , which at the redshift of the galaxy ( $z = 0.055$ ) corresponds to approximately  $400 \text{ pc} \times 400 \text{ pc}$  per pixel. As previously mentioned, we measure a PSF with  $\text{FWHM} = 0''.71$  for the MUSE image.

Sky emissions were removed separately from all galaxy exposures using the sky-field from offset sky-exposures, taking into account the instrumental line spread function for each IFU.

#### 3.2. Treatment of spectra and derivation of (parametric) stellar kinematics

For our study of Holm 15A, we initially used the MUSE absorption spectra to derive spatially resolved, 2D stellar kinematics parameterized by the rotational velocity  $v_{rot}$ , velocity dispersion  $\sigma$  and higher-order Gauss-Hermite coefficients  $h_3$  and  $h_4$  of the line-of-sight velocity distribution (LOSVD). For the dynamical modelling, we use non-parametric LOSVDs that were derived following a set of equivalent steps (see Sec. 3.3).

To achieve a balance between a precise measure of the kinematics in the core and an overall high spatial resolution we aim for a target S/N of at least  $\sim 50$  per pixel in each spectrum. To achieve this, we spatially bin the data cube using the Voronoi tessellation method of Cappellari & Copin (2003). Pixels belonging to foreground

sources such as galaxies or AGN are removed from the data before binning.

At the center of the galaxy ( $r \leq 5$  kpc) the spatial resolution of the Voronoi bins turns out to be  $0.4'' - 0.8''$  (roughly  $400 - 800$  pc) for a  $S/N \sim 50$ . We here define the radius of the gravitational sphere of influence (SOI) of the black hole as the radius where the enclosed mass  $M_*(\leq r_{SOI}) \equiv M_{BH}$ . By integrating the deprojected 3D luminosity density and assuming a range of plausible stellar mass-to-light ratios, between  $\Upsilon_* = 4$  and 6, we estimated the enclosed mass of the galaxy. For the lowest expected black hole mass for a galaxy of this mass and velocity dispersion,  $M_{BH} = 3 \times 10^9 M_\odot$  (cf. Section 1), the enclosed stellar mass equals  $M_{BH}$  at  $r_{SOI} \sim 1''.6$ . Hence, with a diameter of  $2 \times 1''.6 = 3''.2$  our PSF and spatial binning resolution, which are both on the order  $0''.8$  ensure that we can resolve the expected sphere of influence (SOI) by a factor  $\geq 4$ . As discussed above, the extreme core properties of Holm 15A actually point to a SMBH with  $M_{BH} \sim 10^{11} M_\odot$ , whose SOI radius would be roughly  $r_{SOI} \sim 4 - 5''$  – a factor  $> 10$  above our resolution limit. If the dark matter halo is included in the modeling, this resolution is sufficient for a robust black hole mass determination (Rusli et al. 2013b).

In total, we obtain 421 spatial bins, of which 145 bins are located inside the central  $5''$ .

For the purpose of our subsequent dynamical modeling of the galaxy we divided the spatial bins of our MUSE FOV into four quadrants, q1-4 in such a way that quadrant membership is determined by which side of the major and minor axes the center of each bin is located on

Parametric LOSVDs for each bin were obtained by fitting the stellar absorption lines of the galaxy with Penalized Pixel-Fitting (pPXF, Cappellari 2017) implemented in Python 2.7. PPXF convolves a weighted sum of template stellar spectra, in this case the MILES library (Sánchez-Blázquez et al. 2006) with a Gauss-Hermite LOSVD in order to fit the absorption features. Optionally, emission-line features of ionized gas are fit simultaneously, with a separate set of templates and LOSVDs. Figure 5 shows an example of a (parametric) kinematic fit to the spectral features of Holm 15A with pPXF for a bin located roughly  $0''.5$  from the center of the galaxy (best fit to stellar component:  $v_{rot} = -1.59 \pm 8.04$  km/s relative to the systemic velocity of the galaxy,  $\sigma = 342 \pm 9.71$  km/s,  $h_3 = 0.025 \pm 0.015$ ,  $h_4 = 0.062 \pm 0.018$ ).

Several bins within the central 5 kpc of the galaxy – primarily in the southeastern regions – region contain emission lines from ionized gas, most notably  $H\alpha$ ,  $H\beta$ , [OIII] 5007 Å, [NI] 5199 Å and [NII] 6583 Å (cf.

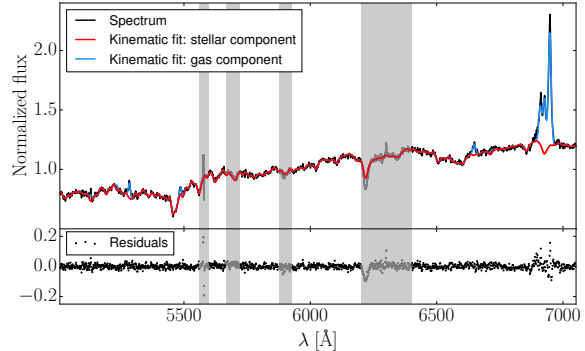


**Figure 5.** Stellar kinematic fit with pPXF (red) to a normalized spectrum of Holm 15A (black) with corresponding residuals (black points, lower panel). Emission lines from ionized gas are fit simultaneously (blue). Spectral regions masked during the fit are shown as gray shaded areas.

Figure 5), which we fitted with the emission line fitting routine of pPXF, though we do not consider their kinematics in this study. Figure 6 shows the measured emission line flux for  $H\alpha$ ,  $H\beta$ , [OIII] and [NII]. The average flux ratios  $\log([OIII]/H\beta) = 0.09 \pm 0.26$  and  $\log([NII]/H\alpha) = 0.48 \pm 0.12$  of emission lines with  $S/N > 3$  are associated with LINER-type emission (Kauffmann et al. 2003), which is quite typical for cool-core clusters. Of the 100 brightest X-ray clusters, Abell 85’s cool core has the 14th strongest cooling flows (Chen et al. 2007). The spatial extent of this LINER-type emission ( $\sim 4 - 5$  kpc) suggests it could be related to ionized cooling-flow filaments (e.g Ferland et al. 2008, 2009; Ogrea et al. 2010). This was already previously noted by McDonald et al. (2010), who found that it coincided with a similarly extended region of X-ray emission associated with cooling flows.

By contaminating some absorption features such as  $H\beta$ , the gas emission increase the uncertainties of the kinematic fits in some bins. As we will show in section 4, this contamination of mostly central spectra slightly increases the uncertainty of  $M_{BH}$ , but has little impact on the global stellar mass-to-light ratio  $\Upsilon_*$  and the shape of the dark matter halo.

At redshift  $z = 0.055$ , the strong oxygen 5577 Å emission line lies on top of the 5270 Å Fe-feature. Because this line is difficult to remove, the Esoreflex sky subtraction left strong residuals in this region, effectively rendering it unusable for fitting. We noted a few additional systematic residuals which may be related to sky subtraction or telluric correction issues as well. In order to minimize possible systematics in the LOSVDs, we defined one single mask that we used for all spectra throughout the entire galaxy. We consistently mask

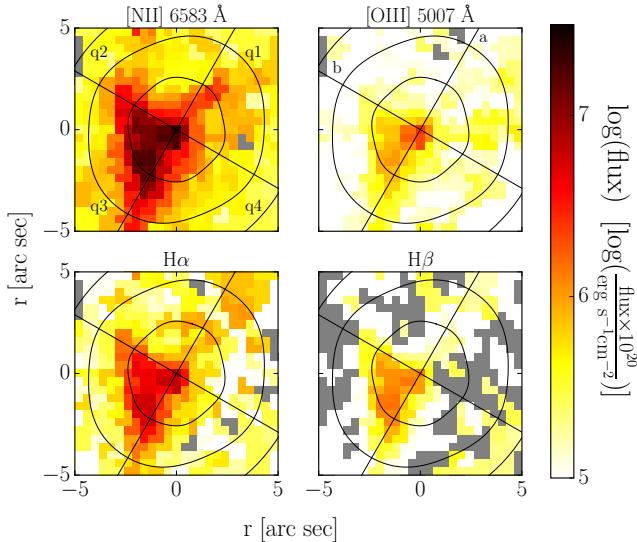


**Figure 6.** Logarithmic flux of emission lines [NII], [OIII], H $\alpha$  and H $\beta$  from ionized gas located within central regions of the galaxy. Grey areas indicate bins for which no meaningful emission line-fit could be derived. Photometric i-band isophotes are shown in black. axes  $a$  and  $b$  (black lines) correspond to the major- and minor axes of the galaxy respectively. The center of the galaxy coincides with the peak of the emission line flux.

all wavelength regions that are possibly affected by any systematic issues.

We performed our kinematic fits over the spectral interval between 5010 and 7050 Å. Including spectral regions bluer than 5010 Å resulted in lower-quality fits and a constant bias in  $h_3$ , indicative of template mismatch. Spectral regions redder than 7050 Å were badly affected by sky lines and were therefore omitted. In particular, we could not derive meaningful kinematics in the [Ca II] triplet region.

We also used a 6th order multiplicative polynomial and an additive constant in the fit. The former allows for the correction of errors in the flux calibration, while the latter is typically used to correct over- or underestimations of the continuum during sky correction. We also made use of the sigma clipping and bias-factor options. The value of the bias factor – 0.2 in our case – was determined from testing pPXF on Monte Carlo simulations of model spectra.

A subset of stellar template spectra for the fit was selected as follows: We fitted a mean spectrum of all bins of the galaxy with the full set of 985 MILES library templates. All binned spectra were corrected for the systematic velocity of the galaxy, as well as their respective rotational velocities. All spectra were normalized to one before averaging. We set both the third-order Gauss-Hermite coefficient  $h_3$  and the additive constant to zero

in order to avoid template mismatch (which can result in biases in these parameters). With these restrictions pPXF assigned non-zero weights exclusively to a set of 16 templates with a wide variety of luminosity classes but limited to spectral types G, K and M, in good agreement with the uniformly red color of the galaxy (ec. 2). We used this subset of stars from the MILES library as templates for fitting the galaxy’s absorption features in all Voronoi bins.

The parameterized kinematics in the interval between 5010 and 7050 Å over the MUSE FOV are shown in Figure 7. As can be seen in the figure, we measure a weak rotation signal of less than 40 km/s, which is only faintly reciprocated in  $h_3$  – the rotation is likely too weak for an anti-correlated signal in this parameter to be detectable. The velocity dispersion  $\sigma$  peaks in the central regions ( $r < 2$  kpc) at  $\sim 350$  km/s, stays somewhat constant at  $\sim 330$  km/s throughout most of the FOV and finally starts to rise again at the edges of the MUSE FOV up to  $\gtrsim 370$  km/s. Our measured velocity dispersions are similar to those of Fogarty et al. (2014). Our  $h_4$  kinematic profile starts out at  $\sim 0.07$  within 2 kpc and rises to  $\gtrsim 0.1$  towards the edges of the FOV. In Appendix A.1 we compare the kinematics of Holm 15A to those of massive ETGs from the MASSIVE survey. The corresponding statistical uncertainties are shown in Figure 8. Uncertainties were determined from Monte Carlo simulations on model spectra of the galaxy, i.e. re-fitting best-fit spectral models with with 100 different noise realizations, the noise being drawn from a Gaussian distribution with a dispersion corresponding to the local S/N, which is measured directly from each spectrum. We note that the distribution of uncertainties is spatially asymmetric between central bins across quadrants – central kinematics in q3 have overall larger uncertainties than those in the other quadrants. This is in agreement with the distribution of emission-line flux between quadrants (cf. Figure 6), i.e. q3 seems to be affected worse by uncertainties introduced by gas contamination of absorption features. As we will show in Section 4, including q3 in our dynamical modeling increases the uncertainty of our  $M_{BH}$  determination.

We had previously also acquired spectroscopy of Holm 15A from the McDonald Observatory using the low-resolution mode ( $\sigma \sim 25$  km/s) of the integral field unit spectrograph VIRUS-W (Fabricius et al. 2012) (on which our proposal for MUSE observations of Holm 15 were based). We find that stellar kinematics determined from this independent set of spectra agree with those from our MUSE data.

### 3.3. Non-Parametric LOSVDs

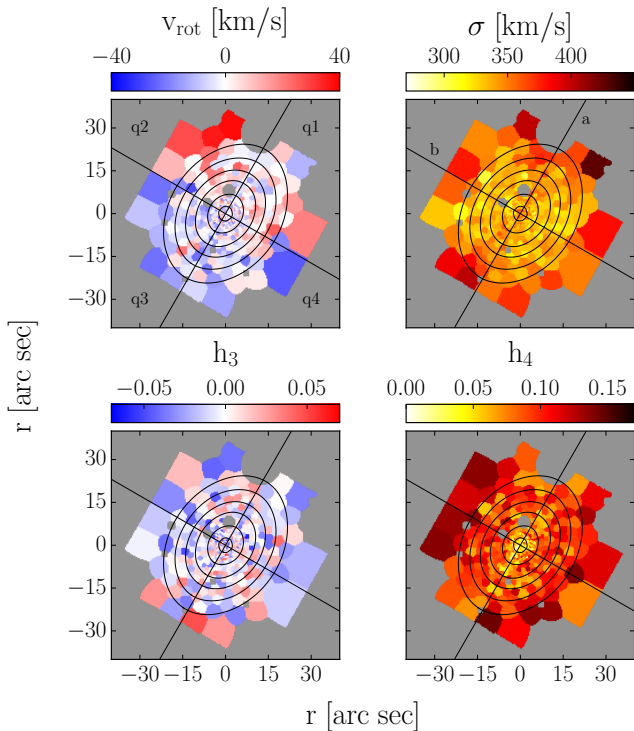


**Figure 7.** From top to bottom, left to right: kinematic maps of the rotational velocity  $v_{rot}$ , velocity dispersion  $\sigma$  and the higher-order Gauss-Hermite coefficients  $h_3$  and  $h_4$  over the MUSE FOV. The systematic velocity of the galaxy has been subtracted in the kinematic map of  $v_{rot}$ . Ellipse fits to i-band isophotes are drawn in black; axes  $a$  and  $b$  (black lines) correspond to the major- and minor axes of the galaxy respectively.

In our dynamical modeling of Holm 15A we set out to achieve a precise mass measurement of the galaxy, which makes the parametric representation of the stellar kinematics in Figure 7 problematic: Large values of  $\sigma$  and  $h_4 > 0$  over the entire FOV result in the escape velocity of the galaxy,  $v_{esc}$  being practically infinite everywhere. Since  $v_{esc}$  depends directly on the gravitational potential we try to measure it as accurately as possible.

To obtain LOSVDs with more realistic  $v_{esc}$ , we use our own kinematic extraction code (Thomas et al. in prep.) which operates in a similar way as pPXF but minimizes the  $\chi^2$  over all spectral pixels by utilizing a Levenberg-Marquardt algorithm to fit a template broadened with a non-parametric LOSVD to the absorption features of a galaxy.

We use the same setup of template stars, additive and multiplicative polynomials as described above. Emission lines are masked for each spectrum individually, according to their respective widths (spectral regions within  $4 \times \sigma_{gas}$  are masked for each emission line) and positions as determined with the pPXF emission line fit. The non-

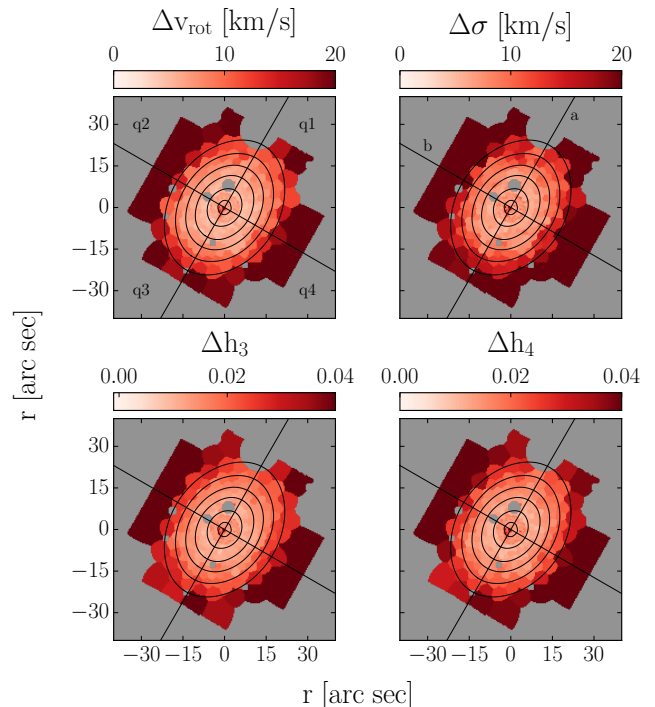


**Figure 8.** Maps of statistical uncertainties corresponding to the parameters of the kinematic maps of Figure 7.

parametric LOSVDs mainly differ from the parametric ones in the high-velocity tails, as demonstrated for an example bin of Holm 15A in Figure 9. While the width of the LOSVD ( $\sigma = 338 \pm 9.57$  km/s with our own code and  $\sigma = 328 \pm 10.7$  km/s with pPXF), as well as its global shape, are similar for both methods, the non-parametric LOSVDs provide a more realistic sampling of the LOSVD and noise at large projected velocities. Therefore, for our dynamical study of Holm 15A, we use the non-parametric LOSVDs. Radial profiles comparing both parametric and non-parametric kinematics for all bins in our study are presented in Appendix A.2.

## 4. SCHWARZSCHILD DYNAMICAL MODELING OF HOLM 15A

### 4.1. Dynamical models

We dynamically modeled Holm 15A under the assumption of axisymmetry. The lack of unambiguous, obvious isopotential distortions (see Section 2) and the overall symmetry of the observed kinematic profiles (see Section 3.2) imply that Holm 15A is generally consistent with an axially symmetric stellar distribution.

The dynamical models in this study were constructed using an updated version of our axisymmetric Schwarzschild orbital superposition code. We will here only briefly summarize the key features of our imple-

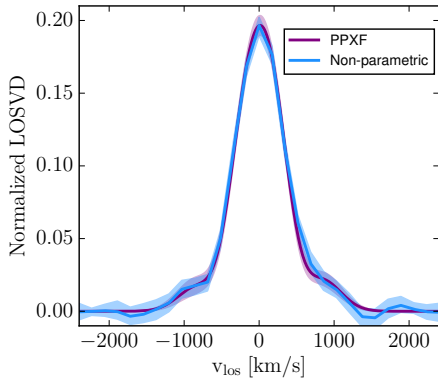


**Figure 9.** Example LOSVD-recoveries from the central regions of q4 originating from two different methods: One determined parametrically with pPXF (purple) and the other non-parametrically with our own code (blue). The shaded envelopes indicate statistical uncertainties.

mentation and refer to previous publications for more in-depth descriptions (Richstone & Tremaine 1988; Gebhardt et al. 2003; Thomas et al. 2004; Siopis et al. 2009).

Schwarzschild dynamical modeling is based on the calculation of stellar orbital distributions in a fixed gravitational potential as a solution to the collisionless Boltzmann equation (Schwarzschild 1979). Any orbit can be fully described by three integrals of motion: The classical integrals  $E$  and  $L_z$  (in the axisymmetric case) plus a non-classical integral  $I_3$  (in most astrophysically relevant cases). Sampling values of this set of integrals of motion ( $E$ ,  $L_z$ ,  $I_3$ ) allows us to create an orbit library in a given gravitational potential  $\Phi$  whose distribution function  $f(\mathbf{r}, \mathbf{v})$  satisfies the collisionless Boltzmann equation.

In order to determine  $\Phi$ , we assume that the density distribution of Holm 15A can be described by

$$\rho(r, \theta) = \rho_*(r, \theta) + M_{BH}\delta(r) + \rho_{DM}(r), \quad (1)$$

which we insert into Poisson’s equation.  $\rho_*$  is linked to the three dimensional deprojection  $\nu(r, \theta)$  of the observed i-band surface brightness (cf. Section 2) via the stellar (i-band) mass-to-light ratio,  $\rho_*(r, \theta) = \Upsilon_* \cdot \nu(r, \theta)$ , assuming a spatially constant stellar  $\Upsilon_*$ . In addition to the mass of the central black hole  $M_{BH}$ , the model admits the inclusion of a dark matter (DM) halo  $\rho_{DM}(r)$ . Here, we chose a generalised NFW-halo derived from cosmological N-body simulations (Navarro et al. 1996; Zhao 1996):

$$\rho_{DM}(r) = \frac{\rho_0}{\left(1 + \frac{r}{r_s}\right)^{3-\gamma} \left(\frac{r}{r_s}\right)^\gamma}, \quad (2)$$

with

$$\rho_0 = \rho_{10} \left(1 + 10 \frac{\text{kpc}}{r_s}\right)^{3-\gamma} \left(10 \frac{\text{kpc}}{r_s}\right)^\gamma, \quad (3)$$

where  $\rho_{10}$  is the DM density at 10 kpc,  $r_s$  the scale radius of the halo and  $\gamma$  the inner slope of the DM density profile.

For a given  $\Phi$ , we sample thousands of representative initial orbital conditions, implicitly varying all the integrals of motion  $E$ ,  $L_z$  and  $I_3$ , and including individual orbital phase-space volumes (Thomas et al. 2004). For Holm 15A, we stored LOSVDs in 29 velocity bins adapted to the velocity dispersion of the galaxy, with one LOSVD associated with each of the 421 spatial bins of our FOV, meaning our models fitted roughly a total of 3000 velocity bins per quadrant.

We use the NOMAD optimization software (Audet & Dennis, Jr. 2006; Le Digabel 2011; Audet & Hare 2017) to find the set of mass parameters  $M_{BH}$ ,  $\Upsilon_*$ ,  $\rho_{10}$ ,  $r_s$  and  $\gamma$  that yields the best fit to the observed kinematics.

#### 4.2. Results

The most important result from our dynamical modeling is the detection of a SMBH with  $M_{BH} = (4.0 \pm 0.80) \times 10^{10} M_\odot$  in Holm 15A. The associated SOI of this SMBH is  $r_{SOI} = 3.8 \pm 0.37$  kpc ( $3''.5 \pm 0''.34$ ). Even though the galaxy is more than 200 Mpc away, we spatially resolve the SOI by a factor of 10. In fact,  $\sim 100$  out of our 421 LOSVDs sample the SOI of the galaxy. The modeling results for the black hole, stellar mass-to-light ratio and DM halo parameters are summarised in Table 2.  $\Delta\chi^2$  curves for  $M_{BH}$ ,  $\Upsilon_*$  and  $\rho_{10}$  from all four quadrants are shown in Figure 10. The figure shows that none of the four quadrants stands out and yields a significantly different result than the others. While the black hole mass in q3 (where the gas emission in the spectra is most prominent) is slightly larger than in the other quadrants, this offset is not significant. By computing the dynamical quantities separately for each quadrant and estimating the uncertainties from these four nearly independent measurements, we implicitly include any residual systematics (like, e.g., from the gas emission) in our error budget. Fits to the kinematics of one quadrant of Holm 15A parameterized by  $v_{rot}$ ,  $\sigma$ ,  $h3$  and  $h4$  of our best-fit model are shown in Figure 11. They show that our best-fit model can successfully reproduce the observed kinematics of the galaxy. For the non-parametric kinematics our best-fit model reaches a reduced  $\chi^2$  of 0.8 – 0.9 for each quadrant. An example comparison between an observed and modelled LOSVD and a discussion of the importance of the LOSVD wings can be found in Appendix B.

## 5. DISCUSSION

With  $M_{BH} = (4.0 \pm 0.80) \times 10^{10} M_\odot$ , the SMBH at the center of Holm 15A is the most massive dynamically determined black hole so far. It is a factor of

Schwarzschild Model Parameter	Best-Fit Value	Units
$M_{BH}$	$(4.0 \pm 0.80)$	$10^{10} M_{\odot}$
$\Upsilon_{\star}$ (i-band)	$4.5 \pm 0.19$	
DM Halo:		
$\rho_{10}$	$(1.0 \pm 0.10)$	$10^7 \frac{M_{\odot}}{\text{kpc}^3}$
$\log r_s$	$(2.4 \pm 0.29)$	$\log \frac{r}{\text{kpc}}$
$\gamma$	$0.35 \pm 0.26$	

**Table 2.** Results of Schwarzschild dynamical modeling of Holm 15A. Best-fit values were derived as the mean of the independent fits to the four quadrants. The quoted uncertainties are derived from the variation between quadrants.

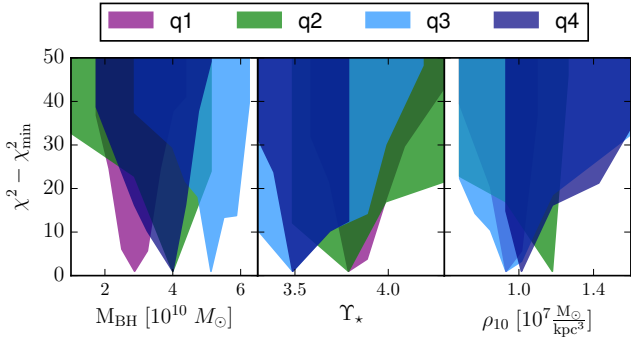


**Figure 10.** From left to right:  $\chi^2$  for our minimization curves of our dynamical modeling for the parameters  $M_{BH}$ ,  $\Upsilon_{\star}$  and  $\rho_{10}$ . Each quadrant (q1-4) was modeled separately. The variation between their respective  $\chi^2$  curves is treated as representative of the inherent systematic and statistical uncertainties of each measurement.

two larger than the SMBHs in NGC 4889 (McConnell et al. 2012a), with  $M_{BH} = (2.1 \pm 0.99) \times 10^{10} M_{\odot}$  and NGC 1600 with  $M_{BH} = (1.7 \pm 0.15) \times 10^{10} M_{\odot}$  (Thomas et al. 2016). Quasar luminosities at higher redshifts and current determinations of local SMBH scaling relations give an expected black hole cumulative space density ranging from half a dozen up to a few hundred SMBHs with  $M_{BH} \gtrsim 10^{10} M_{\odot}$  out to  $z \leq 0.055$  (e.g. Lauer et al. 2007b; Rusli et al. 2013b). Hence, circumstances for the formation of a 40-billion-solar-mass SMBH are probably rare, but the central structure of the Coma cluster serves as an example that they do exist. As stated above, NGC4889, one of the two central galaxies of Coma, contains a SMBH of  $M_{BH} = 2.1 \times 10^{10} M_{\odot}$ . The other galaxy, NGC4874, has a very extended classical shallow-power-law surface-brightness core with a size of  $r_b = 1.7$  kpc (Lauer et al. 2007a). This suggests a SMBH with a mass of  $M_{BH} \sim 2 \times 10^{10} M_{\odot}$  (using the core scaling relations of Thomas et al. 2016). Both galaxies are in interaction and will eventually merge (e.g. Arnaboldi et al. 2006; Gerhard et al. 2007). This will

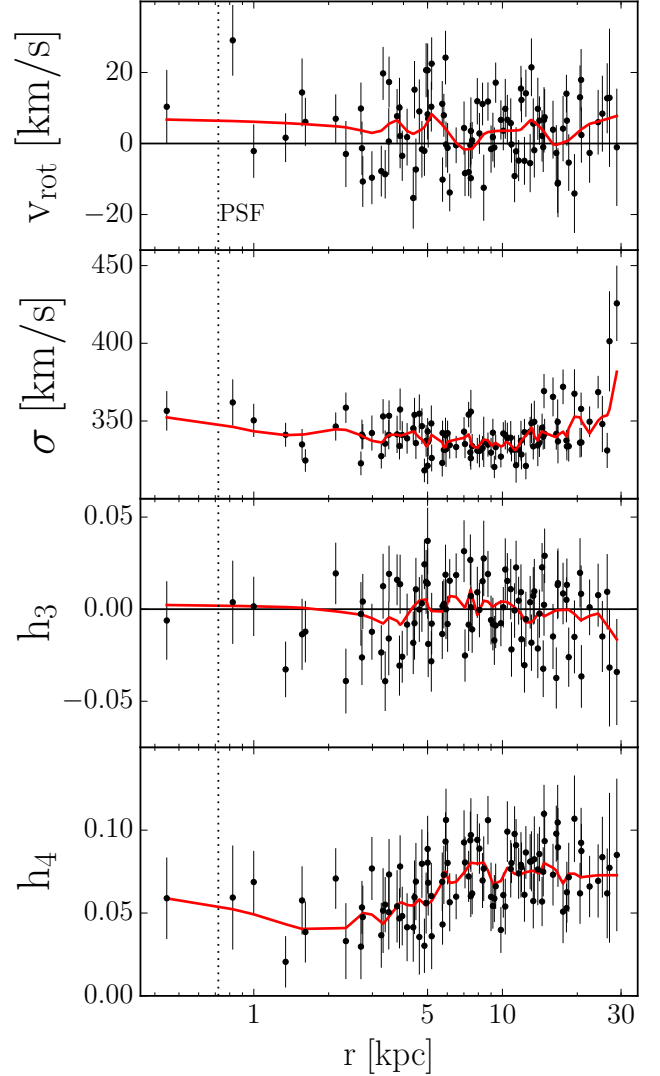


**Figure 11.** Comparison of Gauss-Hermite parameterizations of the kinematic data (black points) and best-fitting model predictions for quadrant q4. Shown are (from top to bottom)  $v_{rot}$ ,  $\sigma$ ,  $h_3$ , and  $h_4$ . Note that the model was fit to the full (non-parametric) LOSVDs from the 2D data, not to the Gauss-Hermite moments plotted in the figure.

produce a BCG at the center of the Coma cluster which will very likely have a SMBH in the same mass range as Holm 15A has now.

In the following we will discuss the observational evidence for a merger origin of Holm 15 and its depleted core in more detail.

### 5.1. Evidence for dissipationless merging and similarity with other core galaxies

The SMBH of Holm 15A is not only the most massive one to date, it is also four to nine times larger than expected given the galaxy's bulge stellar mass  $M_{Bu} =$

$(2.5 \pm 0.64) \times 10^{12} M_{\odot}$  and the galaxy’s stellar velocity dispersion  $\sigma = (346 \pm 12.5) \text{ km/s}$ , relative to  $M_{BH} - M_{Bu}$  scaling relations for cored ETGs from Saglia et al. (2016) and McConnell & Ma (2013) (see Figure 12).

It has been previously noted that the  $M_{BH} - \sigma$  relation is expected to shallow out at the high-mass end due to dry merging dominating over dissipative wet merging as the dominant growth process of massive galaxies. Since dry (major) mergers grow  $\sigma$  only slowly (e.g. Naab et al. 2009) while SMBHs grow linearly (by directly merging with each other), each successive dry merger should displace the merger remnant further towards values of  $M_{BH}$  that are “overmassive” relative to the  $M_{BH} - \sigma$  relation (e.g. Kormendy & Bender 2013). Correspondingly, massive cored galaxies follow a  $M_{BH} - \sigma$  relation that is steeper and slightly offset (towards larger values of  $M_{BH}$  at a given  $\sigma$ ) from the one that less massive, cuspy galaxies follow (cf. Saglia et al. 2016 and McConnell & Ma 2013). Despite the fact that we here already consider these steeper, cores-only relations, Holm 15A is still almost an order of magnitude offset in  $M_{BH}$  from the  $M_{BH} - \sigma$  relation (see Figure 12). This might be indicative of an especially extensive dry merging period.

One could expect the  $M_{BH} - M_{Bu}$  relation to be tighter at the high-mass end, since the ratio  $M_{BH}/M_{Bu}$  ratio is conserved in dry mergers. Holm 15A, however, is also a strong outlier from this relation compared to other cores ( $M_{BH}$  is roughly 4 times larger than expected from  $M_{Bu}$ ). Based on the relation, the ratio between  $M_{BH}$  and  $M_{Bu}$  is expected to essentially be  $\lesssim 0.5\%$  for any cored ETG. Even when including non-cored ETGs, the ratio between  $M_{BH}$  and  $M_{Bu}$  is expected to essentially *always* be  $\lesssim 1\%$  for ETGs of any stellar mass  $< 10^{13} M_{\odot}$ , *irrespective* of central morphology (Kormendy & Ho 2013). Nonetheless, Holm 15A hosts a black hole that contains  $\sim 2\%$  of the total stellar mass of the galaxy, similar to NGC 1600 (Thomas et al. 2016). This might suggest that the progenitor galaxies of Holm 15A were different from massive ETGs at  $z \sim 0$ . Studies of the evolution of  $M_{BH}/M_{Bu}$  from  $z \sim 3$  to 0 via black hole and stellar mass estimates from AGN suggest that the ratio scales like  $(1+z)^{0.7-1.4}$  (e.g. Decarli et al. 2010; Merloni et al. 2010; Bennert et al. 2011). Depending on which  $M_{BH} - M_{Bu}$  relation is used (all central morphologies or cores-only) we can estimate that Holm15A’s progenitors might have formed early at redshifts  $z \gtrsim 1$  or 2

Dissipationless mergers between ETGs involve binary black hole core-scouring and, hence, result in depleted, low-surface-brightness cores. As already mentioned above, core galaxies follow specific scaling relations be-

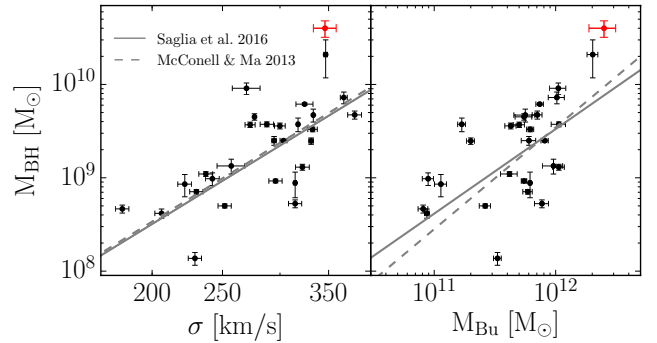


**Figure 12.** Holm 15A (red) compared to cored ETGs listed in Saglia et al. (2016) (black) with respect to the global galaxy scaling relations,  $M_{BH} - \sigma$  (left) and  $M_{BH} - M_{Bu}$  (right). The lines show the linear relations for cored ellipticals from Saglia et al. (2016) and McConnell & Ma (2013).

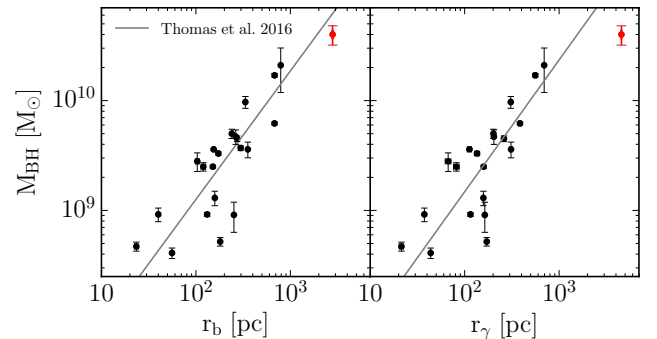


**Figure 13.** Holm 15A (red) compared to cored ETGs from Thomas et al. (2016) and Rusli et al. (2013b,a) (black) with respect to the core-specific scaling relations,  $M_{BH} - r_b$  (left) and  $M_{BH} - r_{\gamma}$  (right). The lines show the linear relations from Thomas et al. (2016). The figure includes the uncertainties of  $r_b$  and  $r_{\gamma}$ , but they are generally smaller than the symbol size.

tween the core size and black-hole mass (Lauer et al. 2007a; Rusli et al. 2013a) or the radius of the sphere-of-influence (Thomas et al. 2016), which can be explained by the black-hole binary model (Rantala et al. 2018). Since the size of the core in Holm 15A is difficult to define we here use both the core-Sérsic break radius  $r_b$  and the cusp radius  $r_{\gamma}$  to compare Holm 15A to other core galaxies (cf. Sec. 2).

In Figure 13 we compare  $r_b$  and  $r_{\gamma}$  from Holm 15A and the sample of core galaxies from Rusli et al. (2013b,a) and compare them with  $M_{bh}$ . We note that values of  $r_b$  and  $r_{\gamma}$  from core-Sérsic profiles for galaxies whose light profiles were originally measured in Lauer et al. (2007a) generally agree with values from the Nuker-profiles listed in that study.

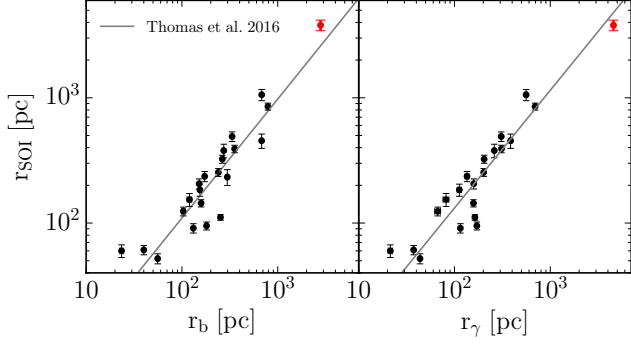


**Figure 14.** Holm 15A (red) compared to cored ETGs from Thomas et al. (2016) and Rusli et al. (2013b,a) (black) with respect to the core-specific scaling relations,  $r_{SOI} - r_b$  (left) and  $r_{SOI} - r_\gamma$  (right). The lines show the linear relations from Thomas et al. (2016). The figure includes the uncertainties of  $r_b$  and  $r_\gamma$ , but they are generally smaller than the symbol size.

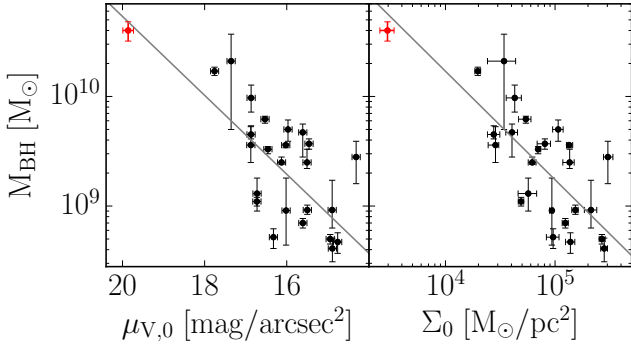


**Figure 15.** The central V-band surface brightness  $\mu_{V,0}$  (left) and stellar surface mass density  $\Sigma_0$  (right) versus  $M_{BH}$  for Holm 15A (red) and cored ETGs from Rusli et al. (2013a,b) and NGC1600 (Thomas et al. 2016) (black). All values of  $\mu_{V,0}$  and  $\Sigma_0$  relate directly to the *observed* light profiles themselves. The line shows the best-fit linear relation.

Evidently, the measured  $M_{BH}$  of Holm 15A is very close to the prediction of the  $M_{BH} - r_b$  relation, while the cusp radius  $r_\gamma$  is much larger than expected.

While this could mean that the break radius from our three-component photometric decomposition is a better parameterization of the core size than the cusp radius, there are also arguments that could explain such an offset towards larger core sizes. For example, if Holm 15A experienced some early accelerated evolution in the past, then it could well be that not only a binary black hole was involved, but possibly a more complicated scenario with multiple black holes. Theory suggests that core scouring efficiency is significantly enhanced by multiple black holes and that cores grow much larger (Kulkarni & Loeb 2012). We will revisit the issue of the offset in  $r_\gamma$  in Sec. 5.2.

In Figure 14 we compare both  $r_b$  and  $r_\gamma$  with the radius of the sphere of influence  $r_{SOI}$ . In this case,  $r_\gamma$  for Holm 15A is perhaps marginally closer to its scaling relation, but both radii are consistent with the correlations between core-size measurements and  $r_{SOI}$  found for other galaxies.

Cores in massive ETGs obey a strong homology in that the central surface brightness correlates inversely with the size of the core (Faber et al. 1997; Lauer et al. 2007b) – This, together with the scaling between  $M_{BH}$  and core size, implies a potential scaling between  $M_{BH}$  and the central stellar surface mass density  $\Sigma_0$ . We show these correlations in Figure 15 for the galaxy sample of Rusli et al. (2013b), NGC1600 (Thomas et al. 2016) and Holm 15A. We used the uncertainties for the stellar mass-to-light ratios and black hole masses listed in Rusli et al. (2013a,b) and (Thomas et al. 2016) and assumed rather conservative uncertainties of  $0.1 \text{ mag/arcsec}^2$  for the light profiles. Our best-fit linear relations were determined following the approach to linear regression from Kelly (2007) (using the Python package *linmix* by Meyers 2015) with errors in both  $M_{BH}$  and  $\mu_{V,0}, \Sigma_0$ :

$$\log(M_{BH}/M_\odot) = (0.36 \pm 0.07)\mu_{V,0}\text{mag}^{-1}\text{arcsec}^2 + (3.53 \pm 1.16) \quad (4)$$

$$\log(M_{BH}/M_\odot) = (-0.99 \pm 0.19)\log(\Sigma_0/M_\odot\text{pc}^{-2}) + (14.19 \pm 0.09). \quad (5)$$

The  $M_{BH} - \mu_{V,0}$  relation has an intrinsic scatter  $\epsilon = 0.32 \pm 0.07$ . Similarly, the  $M_{BH} - \Sigma_0$  relation has an intrinsic scatter of  $0.30 \pm 0.07$ . Values of  $\Sigma_0$  were calculated from the surface brightness at the spatial resolution limit for each galaxy and their corresponding dynamical stellar mass-to-light ratios (Rusli et al. 2013a,b; Thomas et al. 2016). Values for both  $\mu_{V,0}$  and  $\Sigma_0$  were determined using the *observed* light profiles of each core galaxy. Hence, the surface brightnesses/densities are independent of any assumed light profile model. Holm 15A has the lowest central stellar surface brightness/mass,  $\mu_{V,0} = 19.9 \pm 0.13 \text{ mag/arcsec}^2$ ,  $\Sigma_0 = (3.0 \pm 0.40) \times 10^3 M_\odot/\text{pc}^2$  of all core galaxies with dynamical black hole mass measurements (cf. Figure 15). Nonetheless, Holm 15A is fully consistent with the homology established by other core galaxies.<sup>2</sup> All of

<sup>2</sup> The listed relations were determined *including* Holm 15A, but the relations change only marginally and within the listed uncertainties when we don't include the galaxy.

the above evidence points to the fact that the core in Holm 15A was formed by the same physical process as cores in other massive ETGs, i.e. by a black-hole binary.

### 5.2. *N*-body merger simulations: evidence for a merger between two core galaxies

As discussed in Section 2, the central light profile of Holm 15A is nearly exponential, which sets it apart from the typical profiles of other cores. This is despite the fact that the galaxy seems to respect the core scaling relations (see above). We will now discuss what the specific properties of Holm 15A tell us about its merger history.

In Figure 16 we compare the light profile of Holm 15A with the *N*-body merger simulations of Rantala et al. (2018, 2019). These simulations study the outcome of a dissipationless merger between two early-type progenitor galaxies, both with central black holes. The simulations follow the dynamical interaction between the black hole binary that temporarily forms at the center of the remnant galaxy and the surrounding stars with high accuracy. The figure demonstrates that mergers between cuspy progenitors (i.e. mergers between originally coreless progenitor galaxies) lead to slightly different light profiles than do mergers between galaxies that already had cores. The light profile of Holm 15A, in fact, looks very similar to the 2nd type of merger, i.e. between two already cored galaxies<sup>3</sup> (Figure 16).

The evidence in favor of a core-core merger from the light profile is consistent with the evidence from the orbit distribution that we find in Holm 15A. Figure 17 shows the radial profile of the anisotropy parameter

$$\beta = 1 - \frac{\sigma_t^2}{\sigma_r^2}, \quad (6)$$

where  $\sigma_r$  is the radial and  $\sigma_t = \sqrt{(\sigma_\theta^2 + \sigma_\phi^2)}/2$  is the tangential velocity dispersion, computed from the dispersions  $\sigma_\theta$  and  $\sigma_\phi$  in the two angular directions. The figure also includes the results from the numerical *N*-body simulations. It is known that core scouring results in an orbital distribution that is biased increasingly towards tangential orbits ( $\beta < 0$ ) inside the SOI of the black hole as  $r \rightarrow 0$  and increasingly towards radial orbits ( $\beta > 0$ ) outside of it, towards larger radii

<sup>3</sup> At roughly  $8 \times r_\gamma \sim 40$  kpc (for Holm 15A) the surface brightness of the rescaled core-core remnant drops faster than the that Holm 15A. This could be due to the fact that the merger simulations do not include an extended cD halo. Photometric studies of Holm 15A (e.g. Donzelli et al. 2011, Kluge et al. in prep.) suggest an extended stellar envelope starting at  $r \gtrsim 35$  kpc. At radii  $< 8 \times r_\gamma$  the core-core remnant is remarkably similar to Holm 15A.

(e.g. Quinlan & Hernquist 1997; Milosavljević & Merritt 2001; Rantala et al. 2018). Tangential anisotropy around SMBHs has been observed in systems of various masses and morphologies (e.g. Verolme et al. 2002; Gebhardt et al. 2003; Shapiro et al. 2006; Houghton et al. 2006; Gebhardt & Thomas 2009; Gültekin et al. 2009; Krajnović et al. 2009; Siopis et al. 2009; Shen & Gebhardt 2010; van den Bosch & de Zeeuw 2010; Schulze & Gebhardt 2011; Gebhardt et al. 2011; McConnell et al. 2012b; Walsh et al. 2015; Feldmeier-Krause et al. 2017; Thomas et al. 2016). In core galaxies, specifically, the measured anisotropy is extremely homogeneous and intimately linked to the core region and follows very closely the prediction of *N*-body merger simulations (Thomas et al. 2014).

In Holm 15A we see the same behaviour: a change from outer radial anisotropy to inner tangential motions roughly at the sphere of influence radius (which is similar to the core size, see Figure 14). The evidence for this comes from the wings of the observed LOSVDs (cf. App. B). However, the central anisotropy in Holm 15A is milder than observed in other core galaxies, which follow the “cuspy-cuspy” line in Figure 17 (Rantala et al. 2018). This difference is actually expected if the direct progenitors of Holm 15A were not cuspy power-law ellipticals but galaxies that already had cores. In the latter case, the anisotropy in the center is predicted to be very similar to the observed orbital structure of Holm 15A (Rantala et al. 2019)<sup>4</sup>.

Since cores grow with each merger generation, a core-core merger scenario would plausibly explain the fact that the central region of Holm 15A is fainter than the centers of  $\gtrsim 97\%$  of the 164 local ETGs in Lauer et al. (2007a), despite the fact that the galaxy is more luminous than  $\gtrsim 90\%$  of the sample ( $M_V = -23.8 \pm 0.1$ , López-Cruz et al. 2014; see also Figure 15). It would also explain the large core size of Holm 15A.

Moreover, it could even provide a reason for Holm 15A’s large cusp radius (Figure 13). During core scouring, a black hole binary displaces roughly its own mass in stars (e.g. Merritt 2006b). As we have shown in the previous subsection, Holm 15A has an extremely massive BH and the lowest central surface mass/brightness of any known core. One could speculate then, that the buildup

<sup>4</sup> In the *N*-body simulations, the final anisotropy profile of an equal-mass core-core merger is very similar to that of the final orbit distribution after a sequence of minor mergers (Rantala et al. 2019). However, the light profile of Holm 15A is more similar to the core-core merger than to the remnant after repeated minor mergers. Further simulations covering a wider range of initial conditions are needed to confirm the connection between anisotropy, profile shape and merger history.

of stars ejected during successive generations of core scouring might eventually have a significant influence on the light profile at the radii where they are deposited. As mentioned in Section 1, Holm 15A does not only have an extremely faint core but is actually brighter than most other core galaxies in the region adjacent to the core out to  $r \lesssim 10$  kpc (cf. Figure 1). In our photometric decomposition the inner exponential light profile results from the *superposition* of the ring component with a “classical” core power-law profile. In this sense  $r_\gamma$  – since it is derived from the curvature of the *total* light profile – could be biased high, whereas  $r_b$  might be the better estimate of the true underlying core size. We note that the ring component from our photometric decomposition (see Section 2), which might or might not be related to the stars ejected from the center, is located adjacent to the core-region at  $a = 4.3 \pm 0.07$  kpc and has – using our measured  $\Upsilon_* = 4.5$  – a total mass on the order of the SMBH,  $\sim 1.7 \times 10^{10} M_\odot$ , i.e. close to the predicted mass of ejected stars.

A detailed analysis of more N-body simulations would be required to investigate whether the deposition of ejected stars can modify  $r_\gamma$  significantly. Also, it is likely that only in the extreme high mass (deficit) range, the result of scouring near the center and deposition of significant stellar mass at larger radii, leads to notable changes of the light profile. At the moment, Holm 15A is only the first massive ETG with a near-exponential core that has been dynamically investigated in detail. Dynamical models and photometric decompositions of other, similar galaxies could help shedding more light on the questions related to their formation, evolution. Donzelli et al. (2011) identified 27 BCGs with low-Sérsic inner light profiles,  $n < 1.5$ , including Holm 15A. Besides Holm 15A, none of these exponential light profile ETGs were dynamically modeled yet.

In the merger case, Holm 15A represents a dynamically very evolved galaxy that is possibly one merger generation ahead of cored galaxies like NGC4874 and NGC4889 at the center of the Coma cluster. As we showed in the previous subsection, Holm 15A’s high  $M_{BH}/M_{Bu}$  ratio of  $\sim 2\%$  might indicate that the galaxy’s progenitors had already formed at redshifts larger than 1 or 2. Abell 85 has one of the strongest cool-cores among X-ray bright clusters (Chen et al. 2007) and is strongly BCG dominated, with Bautz-Morgan morphological type I (Hudson et al. 2010) such that the central parts of the main cluster in fact might have been subject to a slightly accelerated evolution at some point in the past. Previous X-ray studies of Abell 85 had already suggested that the measured temperature and metallicity maps of the cluster were compatible with an

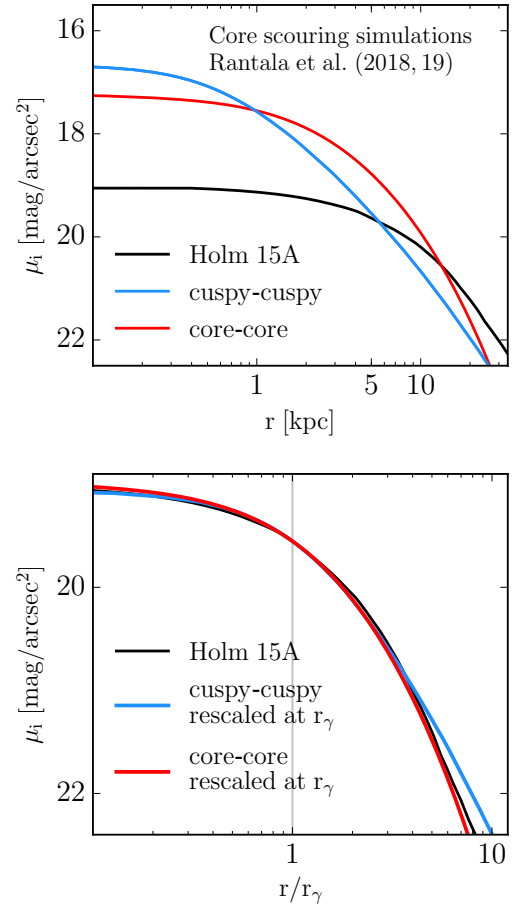


**Figure 16.** Top panel:  $i$ -band surface brightness profile of  $\mu(r)$  of Holm 15A (black) compared to the remnants of numerical merger simulations with core scouring. The blue profile shows a merger between two cuspy galaxies with a final black hole mass of  $M_{BH} = 1.7 \times 10^{10} M_\odot$ , roughly half of the black-hole mass observed in Holm 15A. The red profile is the result of remerging this remnant with itself, doubling the mass of the central black hole to  $M_{BH} = 3.4 \times 10^{10} M_\odot$ . Bottom panel: Holm 15A compared to the remnant surface brightness profiles scaled to the value  $\mu(r \equiv r_\gamma)$  of Holm 15A.

intense merger history (e.g. Durret et al. 2005; McDonald et al. 2010).

### 5.3. Alternative formation scenario via AGN feedback?

Even though the merger scenario provides a consistent explanation for the central light profile shape of the galaxy, the orbital structure and how both are connected to the mass of the central black hole, we briefly discuss whether the interaction between an AGN and the surrounding stars could serve as an alternative core-formation scenario.

In recent simulations, AGN outflows have been observed to trigger fluctuations of the local gravitational potential which irreversibly transfer energy to the dark

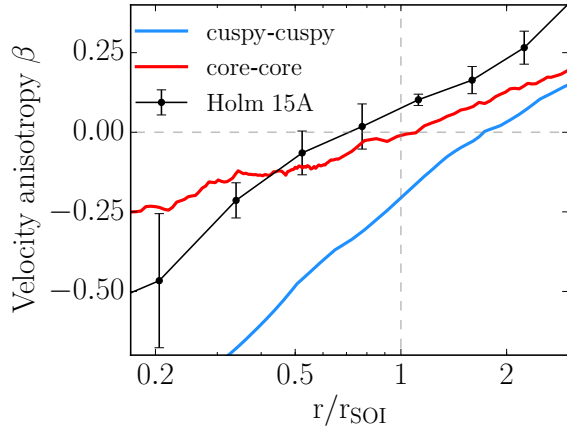


**Figure 17.** Anisotropy profile  $\beta(r)$  of our best-fit dynamical model of Holm 15A averaged over four quadrants compared to numerical merger simulations of binary black hole core scouring from Figure 16, in the same colors as before. Radii are scaled by  $r_{SOI}$ .

matter and stellar components (Teyssier et al. 2011; Martizzi et al. 2012, 2013; Choi et al. 2018). These simulations produced exponential light profiles, which resemble the cores of ETGs in the sense discussed in the introduction: the central surface brightness is low and the slope of the central surface brightness profile is shallow. In fact, based on the black-hole fundamental plane it has been argued that many black holes in the BCGs of cool-core clusters could be more massive than predicted by the classical black-hole scaling relations, and many would actually be expected to have masses  $M_{BH} > 10^{10} M_{\odot}$  (Phipps et al. 2019; Hlavacek-Larrondo et al. 2012). We are still lacking numerical simulations that study in quantitative detail the effect of AGN feedback on the stellar light distribution and orbital structure. The information contained in the actual orbits of the stars might turn out to be crucial to distinguish between different core formation scenarios.

#### 5.4. Dark matter halo and stellar mass-to-light ratio

Figure 18 shows the underlying stellar, dark matter and total enclosed mass and density profiles of our best-fit dynamical model of Holm 15A. Apart from the 20% variation in  $M_{BH}$ , the quadrants of the galaxy produce a consistent overall mass and density profile.

Using simple stellar population models (Thomas et al. 2003; Maraston & Strömbäck 2011) we find that Holm 15A has a marginally super-solar metallicity,  $[Z/H] = 0.08 \pm 0.05$  and is strongly  $\alpha$ -enhanced  $[\alpha/Fe] = 0.25 \pm 0.03$ . Assuming a Kroupa stellar initial mass function (IMF) we find a stellar mass-to-light ratio of  $\Upsilon_{SSP,Kroupa} = 2.7 \pm 0.30$  (i-band) using methods from either Maraston & Strömbäck (2011) or Conroy et al.

(2017). The large  $\sim 20\%$  uncertainty of this value is due to the difficulty of determining the age of the stars. Formally, our SSP models fitted stellar ages that exceed the age of the universe. The value of  $\Upsilon_{SSP,Kroupa}$  and its uncertainty are derived from “manually” varying stellar ages between 10 Gyrs and 13.8 Gyrs while fixing elemental abundances.

Our dynamical mass-to-light ratio of  $\Upsilon_{*} = 4.5 \pm 0.19$  is roughly twice as large as the SSP ratio ( $\Upsilon_{*}/\Upsilon_{SSP,Kroupa} = 1.7 \pm 0.20$ ). This is a continuation of a growing trend among recent mass-to-light ratio measurements in massive ETGs from dynamics, lensing and spectroscopy often finding values larger than predicted by SSP models adopting a Kroupa stellar IMF,  $\Upsilon_{*}/\Upsilon_{SSP,Kroupa} \gtrsim 1.6$  (e.g. Treu et al. 2010; Auger et al. 2010; Thomas et al. 2011; Spiniello et al. 2011; Cappellari et al. 2012; Conroy & van Dokkum 2012; Tortora et al. 2014; Conroy et al. 2017; Parikh et al. 2018; Alton et al. 2018). This offset is roughly consistent with a mass-to-light ratio implied by Salpeter-like IMF or might suggest that DM traces the stars. Our stellar-dynamical mass-to-light ratio is based on the assumption that all mass tracing the galaxy’s light profile belongs to the stars of the galaxy. In this case, when parameterizing the inner DM-halo as  $\rho_{DM} \sim r^{-\eta}$ , we find  $\eta = 0.45 \pm 0.16$  out to roughly 50 kpc. This is substantially shallower than numerical simulations of cold dark matter,  $\eta \geq 1$  (e.g. Navarro et al. 1996, 1997; Moore et al. 1998). Combined stellar kinematics and weak & strong lensing studies of local BCGs previously found  $\rho_{DM} \sim r^{-0.5}$  on scales comparable to the effective radius (e.g. Sand et al. 2004, 2008; Newman et al. 2013).

Within the core region the fraction of DM is  $\lesssim 20\%$ . However, under the assumption of a Kroupa IMF and that DM traces stars, the fraction of DM within the core region would be roughly 50%, while in the former scenario equality between the enclosed stellar and DM mass is reached only at  $r_{eq} = 33 \pm 2.5$  kpc (The stellar mass density profile reaches equality with the DM density profile at  $28 \pm 0.10$  kpc).

In both scenarios the mass density distribution of the stars in our best-fit model has a slope similar to that of the distribution of DM inside the core,  $\rho_{total} \sim r^{-0.5}$ .

We note that some massive galaxies seem consistent with a low-mass IMF (e.g. Thomas et al. 2016; Collier et al. 2018) and that some fine-tuning is required to consistently combine masses from multiple constraints like lensing, dynamics or spectroscopy (e.g. Newman et al. 2017). Dynamical and lensing constraints, in general, become model dependent when stars and DM trace each other closely (e.g. Thomas et al. 2011).

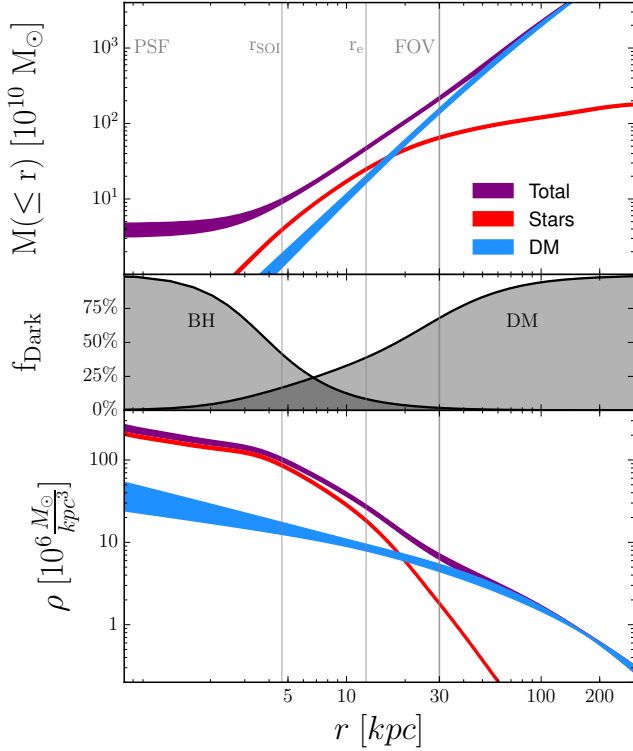


**Figure 18.** Top panel: enclosed mass profile of the best-fit dynamical model of Holm 15A, separated into total (including black hole, purple), stellar (red) and DM (blue) mass. The broadness of the profiles indicates the variation of best-fit models between the quadrants. The middle panel indicates the fraction of non-luminous mass, i.e. the black hole and DM halo, with respect to the total enclosed mass at a given radius for the best-fit model. The bottom panel shows corresponding the stellar, DM and total density distributions.

## 6. SUMMARY AND CONCLUSIONS

We have observed Holm 15A, the BCG of the cool-core galaxy cluster Abell 85, with MUSE. Our observations reveal a galaxy with little rotation ( $v_{rot} < 40$  km/s) and a nearly constant velocity dispersion of  $\sigma = 340$  km/s. Towards the center and towards large radii, the velocity dispersion increases slightly.

By its mass and angular momentum the galaxy falls into the regime of cored ETGs (e.g. Faber et al. 1997; Lauer et al. 2007a; Krajnović et al. 2013), which are commonly described by core-Sérsic light profiles with high Sérsic index  $n$ . However, despite the galaxy’s very diffuse central region, Holm 15A is different from other cored ETGs in having a nearly exponential central light profile. This nearly exponential region encompasses the inner core and the adjacent regions out to  $\sim 10$  kpc, where the galaxy seems to be brighter than most other core galaxies. Formally, this whole region can be well repre-

sented by a central core-Sérsic profile with  $n \approx 1$  and a ring-like extra component adjacent to the core.

We use orbit-based, axisymmetric Schwarzschild models to analyse the dynamical structure of Holm 15A and compare them to recent high-resolution N-body simulations of mergers between ETG galaxies that host black holes. Our results indicate the following:

- Holm 15A hosts a  $(4.0 \pm 0.8) \times 10^{10} M_{\odot}$  SMBH at its center, the most massive black hole directly detected via stellar dynamics so far. It is 4 times larger than expected for the stellar mass of the galaxy.
- Inside of the gravitational sphere of influence of the black hole,  $r_{SOI} = 3.8 \pm 0.37$  kpc, the orbital distribution becomes increasingly tangentially anisotropic. However, the anisotropy inside the core is less tangential than in other big elliptical galaxies with depleted cores.
- The galaxy’s unusual near-exponential and very faint inner light profile and the observed mild orbital anisotropy both match remarkably well with predictions from N-body simulations of a merger between two elliptical galaxies that already had depleted cores.
- The SMBH is roughly 9 times larger than expected from the global  $M_{BH} - \sigma$  relation. At the same time, Holm 15A follows the core-specific scaling relations  $M_{BH} - r_b$  and  $r_{SOI} - r_b$  very well. This supports a merger-driven origin of the galaxy’s extreme core.
- In core galaxies black hole masses scale inversely with the central stellar surface brightness  $\mu_0$  and mass density  $\Sigma_0$  - including in Holm 15A. We show these correlations here for the first time.
- Even when the details of the merging history that led to core formation are unusual, the core-specific  $M_{BH} - r_b$ ,  $r_{SOI} - r_b$ , and  $M_{BH} - \Sigma_0$ ,  $M_{BH} - \mu_0$  correlations are robust. But the light profile and orbital anisotropy contain valuable information about the specific circumstances of core formation.
- Assuming all mass following the light is stellar, we find a bottom-heavy IMF,  $\Upsilon_* = 4.5 \pm 0.19$  (*i*-band), and the inner power-law slope of the DM-density distribution is  $\eta = 0.45 \pm 0.16$ . Equality between enclosed stellar and DM mass is reached at  $33 \pm 2.5$  kpc. Assuming a Kroupa IMF,  $\Upsilon_{SSP, Kroupa} = 2.7 \pm 0.3$ , and DM tracing stars,  $\eta \sim 1$  outside of the core and the fraction of DM within the core is close to 50%.

We plan to extend our analysis of the galaxy to triaxial Schwarzschild models. This will allow us to investigate potential systematics related to symmetry assumptions in the modelling and related to possible substructure near the very center of the galaxy.

Our results suggest that the exact shape of the central light profile as well as the details of the distribution of stellar orbits in the center contain valuable information about the merging history of very massive galaxies. E.g., extreme instances of core formation could potentially lead to remnant surface-brightness profiles diverging from the typical core-Sérsic profiles of “classical” cored galaxies and to the formation of near-exponential cores. Hydrodynamical cosmological simulations have also produced large stellar and dark-matter cores through AGN feedback. It will be interesting to compare the anisotropy profiles predicted by these simulations with measurements in observed galaxies. More extensive simulations are also required to investigate in detail the effect of core scouring under different initial conditions of the progenitor galaxies and on the DM halo.

The SMBH of Holm 15A is a candidate system for direct imaging of its sphere of influence. The photon ring radius is  $\sqrt{27}GM_{BH}/c^2 = 21 \pm 4.1$  AU. At redshift  $z = 0.055$ , this corresponds to an area spanning  $18 \pm 3.7$  mas on the sky, only slightly smaller than the current minimum angular resolution of the Event Horizon Telescope, 25 mas (Event Horizon Telescope Collaboration et al. 2019).

## ACKNOWLEDGEMENT

We acknowledge the support by the DFG Cluster of Excellence "Origin and Structure of the Universe". The dynamical models have been done on the computing facilities of the Computational Center for Particle and Astrophysics (C2PAP) and we are grateful for the support by A. Krukau and F. Beaujean through the C2PAP. We are grateful to Hans Böhringer for valuable discussions and suggestions.

## APPENDIX

### A. STELLAR KINEMATICS

#### A.1. Kinematics of Holm 15A compared to MASSIVE survey ETGs

To better understand Holm 15A’s place among other known massive ETGs we will compare its stellar kinematics to ETGs from the MASSIVE survey (Ma et al. 2014, and subsequent MASSIVE survey papers). Characterizing Holm15 A’s velocity dispersion profile,  $\sigma(r)$  (see Section 3.2) by fitting a combined power-law profile as suggested by Veale et al. (2018) in their study of the 90 ETGs of the MASSIVE survey, we find an inner logarithmic slope  $\gamma_{inner} = -0.017 \pm 0.007$  of the  $\sigma$  profile at  $\sim 2$  kpc and an outer logarithmic slope  $\gamma_{outer} = 0.029 \pm 0.009$  at  $\sim 20$  kpc. Roughly 90% of BCGs in the MASSIVE survey have  $\gamma_{inner} \leq 0$  and  $\sim 60\%$  with  $\gamma_{outer} \geq 0$ . Moreover, for the eleven most massive BCGs in their sample with  $M_* \sim 10^{12}M_\odot$ ,  $\gamma_{inner} \leq 0$  and  $\gamma_{outer} \geq 0$  for all except one. The scatter in  $\gamma_{inner}$  and  $\gamma_{outer}$  between these eleven most massive BCGs is quite high,  $\bar{\gamma}_{inner} = -0.040 \pm 0.055$  and  $\bar{\gamma}_{outer} = 0.088 \pm 0.084$ . Nonetheless, statistically, their overall rather flat  $\sigma(r)$  profiles are similar to the one in Holm 15A, even though the galaxy’s average velocity dispersion within one effective radius  $\sigma_e \sim 340$  km/s is slightly higher compared to these BCGs  $\sim 300$  km/s.

The parameter  $h_4$ , in our measured kinematic profile starts out at  $\sim 0.07$  within 2 kpc and rises to  $\gtrsim 0.1$  along the major axis towards the edges of the MUSE FOV. All 11 of the most massive MASSIVE BCGs share this trend of  $h_4 > 0$  over their respective radial coverage and all but one have positive  $h_4$  gradients towards larger radii. Similarly as with  $\sigma$ , average values for  $h_4$  within  $r_e$  are larger for Holm 15A,  $h_{4,e} \sim 0.08$  than for those other BCGs where  $h_{4,e} \lesssim 0.06$ . Essentially all galaxies in the MASSIVE sample with  $h_{4,e} > 0.05$  (BCG or not) have within the central 2 kpc super-solar  $[\alpha/Fe] > 0.2$  and most galaxies with  $h_{4,e} > 0$  have  $[Fe/H] \leq 0$  (Greene et al. 2019).

Using stellar population models of Lick indices (Thomas et al. 2003; Maraston & Strömbäck 2011) we find abundance ratios in good agreement with these in Holm 15A:  $[\alpha/Fe] = 0.25 \pm 0.03$  and  $[Fe/H] = -0.011 \pm 0.008$ .

Overall, we find stellar kinematics in Holm 15A similar to those of other known massive ETGs. Indeed, from a stellar-kinematic point of view we find no indication that Holm 15A is anything other than a higher-mass extrapolation of known massive ETGs in the local universe, the vast majority of which is cored (e.g. Lauer et al. 2007a; Krajnović et al. 2013; Kormendy & Ho 2013).

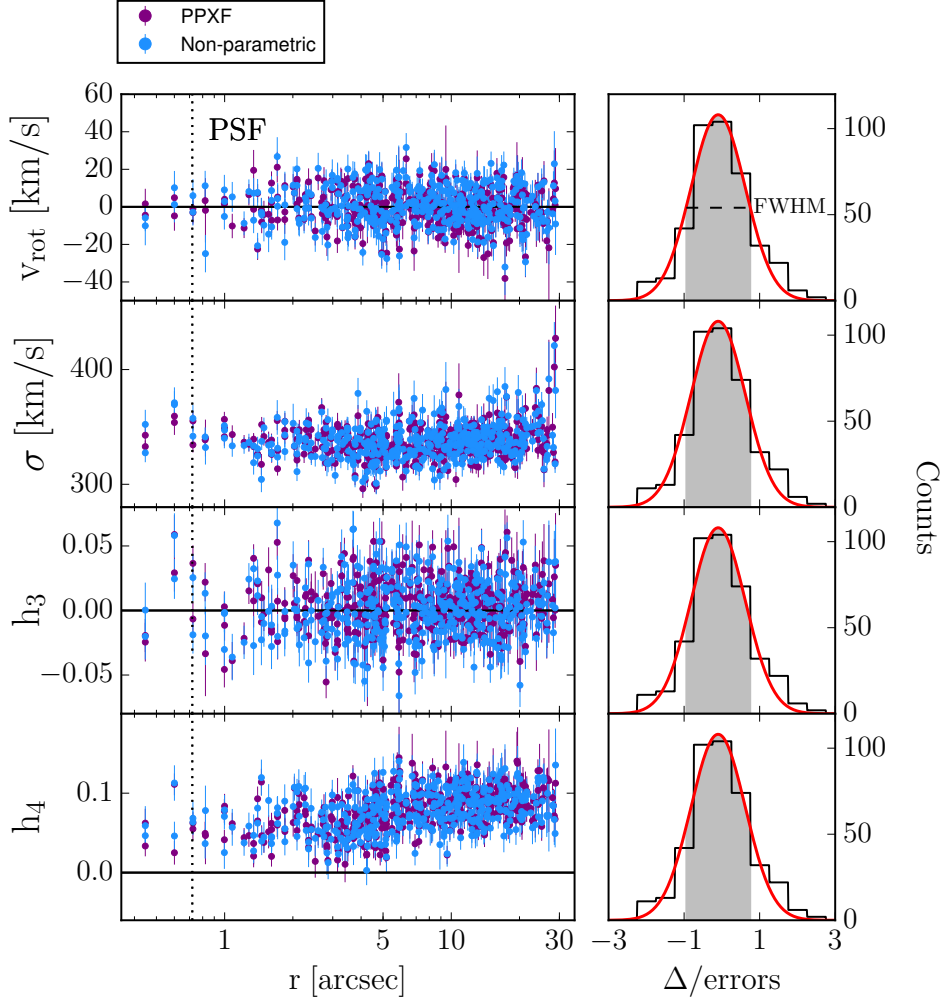


**Figure 19.** Left column: Resulting kinematic profiles over radius of the two kinematic measurements performed in this study, one using pPXF (purple points) and one with our own non-parametric code (blue points). Panels show, from top to bottom, radial profiles for  $v_{rot}$ ,  $\sigma$ ,  $h_3$  and  $h_4$ , including statistical uncertainties. For this plot non-parametric LOSVDs were fitted with a Gaussian times third to fourth order Gauss-Hermite polynomials. In our final modeling non-parametric LOSVDs are used, but these parameters still allow us to showcase the kinematic structure of Holm 15A. Right column, from top to bottom: Corresponding distributions of the difference  $\Delta$  (black) between pPXF and non-parametric LOSVD Gauss-Hermite parameters over the statistical uncertainties of the pPXF values. Each distribution is fit with a Gaussian (red) with the FWHM of each distribution indicated by gray shaded areas.

### A.2. Non-parametric kinematics compared to pPXF

We compare the non-parametric stellar kinematics we measured with our own code with those derived parametrically with pPXF. This is illustrated in Figure 19 for all bins of our FOV (i.e. LOSVDs from all quadrants). Both kinematic profiles are, for the purpose of illustration, parameterized via Gaussian times third to fourth order Gauss-Hermite polynomials. As the distribution of differences in the right column of the figure show, both methods agree within their uncertainties, everywhere.

## B. NON-PARAMETRIC DYNAMICAL MODELING: ESCAPE VELOCITIES

Here, we will briefly discuss the connection between the wings of the observed line-of-sight velocity distributions on the one side and the mass distribution and orbital structure on the other. Figure 20 shows an example of a non-parametric LOSVD measured near the center of Holm 15A together with the corresponding LOSVD from our best-fit dynamical model. We define the cutoff velocity  $v_0$  of any LOSVD as the mean  $v_0 = (v_{0,+} + v_{0,-})/2$ . If  $v_{peak}$  denotes the line-of-sight velocity at which the LOSVD peaks, then  $v_{0,+}$  is the smallest zero of the LOSVD for  $v_{los} > v_{peak}$  and

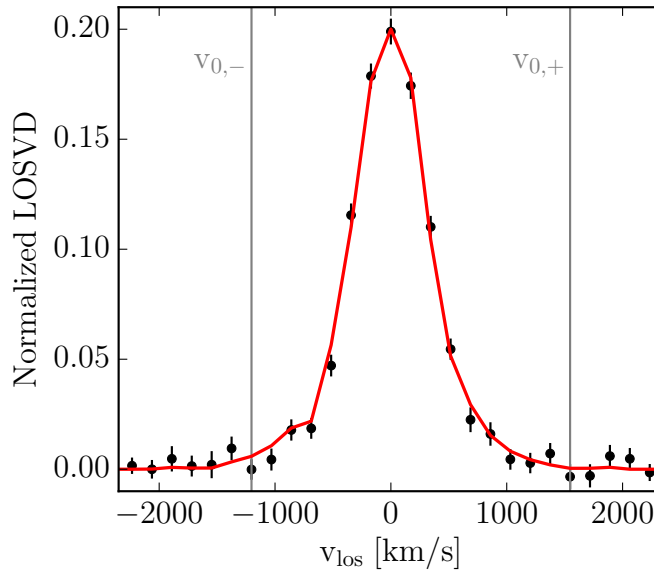


**Figure 20.** Example of a non-parametric fit of our dynamical model (red line) to a non-parametric LOSVD from the center of Holm 15A (black points). The cutoff velocities of the LOSVD are marked as gray, vertical lines.

$v_{0,-}$  is the absolute value of the largest zero of the LOSVD for  $v_{\text{los}} < v_{\text{peak}}$ , respectively. For Holm 15A this definition is sufficient since there is almost no detectable rotation and the LOSVDs are largely symmetric with respect to  $v_{\text{peak}}$ . For the LOSVD in Figure 20 we measure  $v_0 \sim 1375$  km/s.

Figure 21 shows all the measured cutoff velocities  $v_0$  from our MUSE observations together with the escape velocity curves  $v_{\text{esc}}(r)$  of the four best-fit models for the four quadrants of the galaxy. Here, we define  $v_{\text{esc}}$  relative to the maximum radius that is sampled by the orbit library. The uncertainties of the cutoff velocities are measured via the difference between values of  $v_0$  determined from  $LOSVD(v_{\text{los}}) + \Delta LOSVD(v_{\text{los}})$  and  $LOSVD(v_{\text{los}}) - \Delta LOSVD(v_{\text{los}})$ . Outside the core ( $r \gtrsim 5$  kpc), the best-fit  $v_{\text{esc}}(r)$  curves follow closely the maximum observed cutoff velocities  $v_0$ . This is expected in a radially anisotropic system where a significant number of stars is populated on weakly bound, radially extended orbits. The less bound and the more radial the orbit is, the closer the orbital velocity gets to  $v_{\text{esc}}$ . Indeed, outside the core region, our best-fit models become increasingly radially anisotropic (cf. Figure 17).

The situation changes towards the center of the galaxy, where the gravitational well is deepest. The observed cutoff velocities *decrease* at small radii, whereas the escape velocity necessarily increases. This can only be explained as an anisotropy effect: inside the sphere-of-influence of the central black hole (indicated by the vertical line), the orbit distribution becomes tangential (cf. figure 17). Since only stars on the most radial orbits can move with velocities up to the escape velocity and those stars are missing, the LOSVDs do not extend to  $v_{\text{esc}}$  anymore but vanish at smaller velocities.

The uncertainties in the observed cutoff velocities are large (due to the noise in the wings of the LOSVDs). This is indicated by the large scatter in values of  $v_0$ . However, the figure clearly demonstrates the importance of the information contained in the wings of the LOSVDs for both the gravitational potential as well as for the orbital structure.

## REFERENCES

- Alton, P. D., Smith, R. J., & Lucey, J. R. 2018, MNRAS, 478, 4464
- Arnaboldi, M., Gerhard, O., Freeman, K. C., et al. 2006, in IAU Symposium, Vol. 234, Planetary Nebulae in our Galaxy and Beyond, ed. M. J. Barlow & R. H. Méndez, 337–340
- Audet, C., & Dennis, Jr., J. 2006, SIAM Journal on Optimization, 17, 188
- Audet, C., & Hare, W. 2017, Derivative-Free and Blackbox Optimization, Springer Series in Operations Research and Financial Engineering (Springer International Publishing), 302, doi:10.1007/978-3-319-68913-5

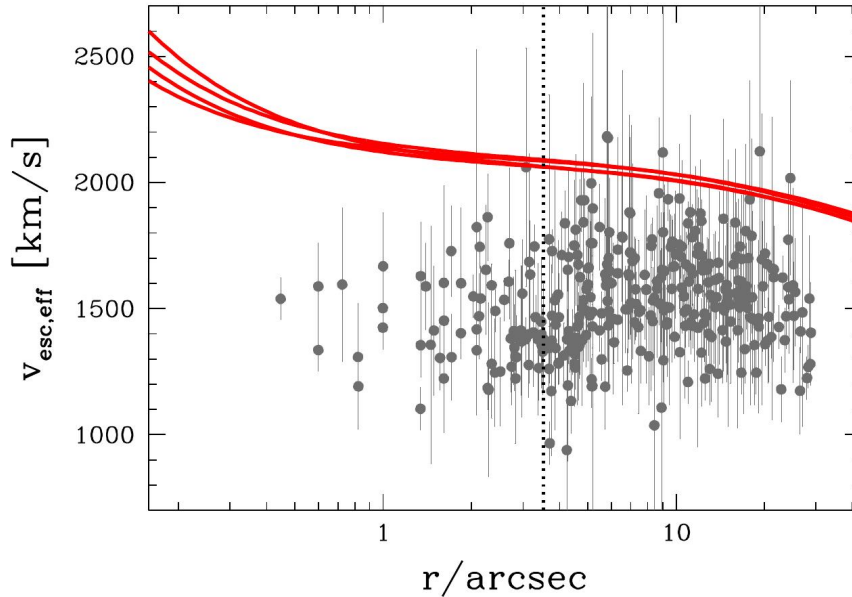


**Figure 21.** Effective escape velocities measured for every LOSVD of our FOV (grey points) and the escape velocities of the gravitational potential of our best fit dynamical model of Holm 15A (4 red lines, one for each quadrant) versus radius. The vertical dotted line indicates the SOI of the black hole.

- Auger, M. W., Treu, T., Gavazzi, R., et al. 2010, *ApJL*, 721, L163
- Begelman, M. C., Blandford, R. D., & Rees, M. J. 1980, *Nature*, 287, 307
- Bennert, V. N., Auger, M. W., Treu, T., Woo, J.-H., & Malkan, M. A. 2011, *ApJ*, 742, 107
- Bonfini, P., Dullo, B. T., & Graham, A. W. 2015, *ApJ*, 807, 136
- Boylan-Kolchin, M., Ma, C.-P., & Quataert, E. 2006, *MNRAS*, 369, 1081
- Cappellari, M. 2016, *ARA&A*, 54, 597
- . 2017, *MNRAS*, 466, 798
- Cappellari, M., & Copin, Y. 2003, *MNRAS*, 342, 345
- Cappellari, M., McDermid, R. M., Alatalo, K., et al. 2012, *Nature*, 484, 485
- Carter, D. 1978, *MNRAS*, 182, 797
- Chen, Y., Reiprich, T. H., Böhringer, H., Ikebe, Y., & Zhang, Y. Y. 2007, *A&A*, 466, 805
- Choi, E., Somerville, R. S., Ostriker, J. P., Naab, T., & Hirschmann, M. 2018, *ApJ*, 866, 91
- Collier, W. P., Smith, R. J., & Lucey, J. R. 2018, *MNRAS*, 478, 1595
- Conroy, C., & van Dokkum, P. G. 2012, *ApJ*, 760, 71
- Conroy, C., van Dokkum, P. G., & Villaume, A. 2017, *ApJ*, 837, 166
- De Lucia, G., Springel, V., White, S. D. M., Croton, D., & Kauffmann, G. 2006, *MNRAS*, 366, 499
- Decarli, R., Falomo, R., Treves, A., et al. 2010, *MNRAS*, 402, 2453
- Donzelli, C. J., Muriel, H., & Madrid, J. P. 2011, *ApJS*, 195, 15
- Durret, F., Lima Neto, G. B., & Forman, W. 2005, *A&A*, 432, 809
- Ebisuzaki, T., Makino, J., & Okumura, S. K. 1991, *Nature*, 354, 212
- Emsellem, E., Cappellari, M., Krajnović, D., et al. 2011, *MNRAS*, 414, 888
- Erwin, P. 2015, *ApJ*, 799, 226
- Event Horizon Telescope Collaboration, Akiyama, K., Alberdi, A., et al. 2019, *ApJL*, 875, L4
- Faber, S. M., Dressler, A., Davies, R. L., et al. 1987, in *Nearly Normal Galaxies. From the Planck Time to the Present*, ed. S. M. Faber, 175–183
- Faber, S. M., Tremaine, S., Ajhar, E. A., et al. 1997, *AJ*, 114, 1771
- Fabricius, M. H., Grupp, F., Bender, R., et al. 2012, in *Society of Photo-Optical Instrumentation Engineers (SPIE) Conference Series*, Vol. 8446, *Proc. SPIE*, 84465K
- Feldmeier-Krause, A., Zhu, L., Neumayer, N., et al. 2017, *MNRAS*, 466, 4040
- Ferland, G. J., Fabian, A. C., Hatch, N. A., et al. 2008, *MNRAS*, 386, L72
- . 2009, *MNRAS*, 392, 1475
- Ferrarese, L., van den Bosch, F. C., Ford, H. C., Jaffe, W., & O’Connell, R. W. 1994, *AJ*, 108, 1598
- Fogarty, L. M. R., Scott, N., Owers, M. S., et al. 2014, *MNRAS*, 443, 485

- Freudling, W., Romaniello, M., Bramich, D. M., et al. 2013, *A&A*, 559, A96
- Fukugita, M., Shimasaku, K., & Ichikawa, T. 1995, *PASP*, 107, 945
- Gebhardt, K., Adams, J., Richstone, D., et al. 2011, *ApJ*, 729, 119
- Gebhardt, K., & Thomas, J. 2009, *ApJ*, 700, 1690
- Gebhardt, K., Richstone, D., Tremaine, S., et al. 2003, *ApJ*, 583, 92
- Gerhard, O., Arnaboldi, M., Freeman, K. C., et al. 2007, *A&A*, 468, 815
- Graham, A. W., Erwin, P., Trujillo, I., & Asensio Ramos, A. 2003, *AJ*, 125, 2951
- Greene, J. E., Veale, M., Ma, C.-P., et al. 2019, *ApJ*, 874, 66
- Gültekin, K., Richstone, D. O., Gebhardt, K., et al. 2009, *ApJ*, 695, 1577
- Hills, J. G., & Fullerton, L. W. 1980, *AJ*, 85, 1281
- Hlavacek-Larrondo, J., Fabian, A. C., Edge, A. C., & Hogan, M. T. 2012, *MNRAS*, 424, 224
- Houghton, R. C. W., Magorrian, J., Sarzi, M., et al. 2006, *MNRAS*, 367, 2
- Hudson, D. S., Mittal, R., Reiprich, T. H., et al. 2010, *A&A*, 513, A37
- Jedrzejewski, R. I. 1987, *MNRAS*, 226, 747
- Kauffmann, G., Heckman, T. M., Tremonti, C., et al. 2003, *MNRAS*, 346, 1055
- Kelly, B. C. 2007, *ApJ*, 665, 1489
- Khochfar, S., & Burkert, A. 2003, *ApJL*, 597, L117
- Kormendy, J. 1985, *ApJL*, 292, L9
- Kormendy, J., & Bender, R. 2009, *ApJL*, 691, L142
- . 2013, *ApJL*, 769, L5
- Kormendy, J., & Ho, L. C. 2013, *ARA&A*, 51, 511
- Kosyra, R., Gössl, C., Hopp, U., et al. 2014, *Experimental Astronomy*, 38, 213
- Krajnović, D., McDermid, R. M., Cappellari, M., & Davies, R. L. 2009, *MNRAS*, 399, 1839
- Krajnović, D., Karick, A. M., Davies, R. L., et al. 2013, *MNRAS*, 433, 2812
- Kulkarni, G., & Loeb, A. 2012, *MNRAS*, 422, 1306
- Lauer, T. R. 1985, *ApJ*, 292, 104
- Lauer, T. R., Ajhar, E. A., Byun, Y.-I., et al. 1995, *AJ*, 110, 2622
- Lauer, T. R., Gebhardt, K., Faber, S. M., et al. 2007a, *ApJ*, 664, 226
- Lauer, T. R., Faber, S. M., Richstone, D., et al. 2007b, *ApJ*, 662, 808
- . 2007c, *ApJ*, 662, 808
- Le Digabel, S. 2011, *ACM Transactions on Mathematical Software*, 37, 1
- López-Cruz, O., Añorve, C., Birkinshaw, M., et al. 2014, *ApJL*, 795, L31
- Ma, C.-P., Greene, J. E., McConnell, N., et al. 2014, *ApJ*, 795, 158
- Madrid, J. P., & Donzelli, C. J. 2016, *ApJ*, 819, 50
- Magorrian, J. 1999, *MNRAS*, 302, 530
- Maraston, C., & Strömbäck, G. 2011, *MNRAS*, 418, 2785
- Martizzi, D., Teyssier, R., & Moore, B. 2013, *MNRAS*, 432, 1947
- Martizzi, D., Teyssier, R., Moore, B., & Wentz, T. 2012, *MNRAS*, 422, 3081
- McConnell, N. J., & Ma, C.-P. 2013, *ApJ*, 764, 184
- McConnell, N. J., Ma, C.-P., Murphy, J. D., et al. 2012a, *ApJ*, 756, 179
- . 2012b, *ApJ*, 756, 179
- McDonald, M., Veilleux, S., Rupke, D. S. N., & Mushotzky, R. 2010, *ApJ*, 721, 1262
- Merloni, A., Bongiorno, A., Bolzonella, M., et al. 2010, *ApJ*, 708, 137
- Merritt, D. 2006a, *ApJ*, 648, 976
- . 2006b, *ApJ*, 648, 976
- . 2013, *Dynamics and Evolution of Galactic Nuclei*
- Merritt, D., & Milosavljević, M. 2005, *Living Reviews in Relativity*, 8, doi:10.12942/lrr-2005-8
- Meyers, J. 2015, *linmix*, <https://github.com/jmeyers314/linmix>, GitHub
- Milosavljević, M., & Merritt, D. 2001, *ApJ*, 563, 34
- Moore, B., Governato, F., Quinn, T., Stadel, J., & Lake, G. 1998, *ApJL*, 499, L5
- Naab, T., Johansson, P. H., & Ostriker, J. P. 2009, *ApJL*, 699, L178
- Naab, T., Khochfar, S., & Burkert, A. 2006, *ApJL*, 636, L81
- Navarro, J. F., Frenk, C. S., & White, S. D. M. 1996, *ApJ*, 462, 563
- Navarro, J. F., Frenk, C. S., & White, S. D. M. 1997, *ApJ*, 490, 493
- Newman, A. B., Smith, R. J., Conroy, C., Villaume, A., & van Dokkum, P. 2017, *ApJ*, 845, 157
- Newman, A. B., Treu, T., Ellis, R. S., & Sand, D. J. 2013, *ApJ*, 765, 25
- Ogrea, G. A., Hatch, N. A., Simionescu, A., et al. 2010, *MNRAS*, 406, 354
- Oser, L., Ostriker, J. P., Naab, T., Johansson, P. H., & Burkert, A. 2010, *ApJ*, 725, 2312
- Parikh, T., Thomas, D., Maraston, C., et al. 2018, *MNRAS*, 477, 3954
- Phipps, F., Bogdán, Á., Lovisari, L., et al. 2019, *ApJ*, 875, 141
- Planck Collaboration, Aghanim, N., Akrami, Y., et al. 2018, *arXiv e-prints*, arXiv:1807.06209

- Postman, M., Lauer, T. R., Donahue, M., et al. 2012, *ApJ*, 756, 159
- Quinlan, G. D., & Hernquist, L. 1997, *NewA*, 2, 533
- Rantala, A., Johansson, P. H., Naab, T., Thomas, J., & Frigo, M. 2018, *ApJ*, 864, 113
- . 2019, *ApJL*, 872, L17
- Richstone, D. O., & Tremaine, S. 1988, *ApJ*, 327, 82
- Rusli, S. P., Erwin, P., Saglia, R. P., et al. 2013a, *AJ*, 146, 160
- Rusli, S. P., Thomas, J., Saglia, R. P., et al. 2013b, *AJ*, 146, 45
- Saglia, R. P., Opitsch, M., Erwin, P., et al. 2016, *ApJ*, 818, 47
- Sánchez-Blázquez, P., Peletier, R. F., Jiménez-Vicente, J., et al. 2006, *MNRAS*, 371, 703
- Sand, D. J., Treu, T., Ellis, R. S., Smith, G. P., & Kneib, J.-P. 2008, *ApJ*, 674, 711
- Sand, D. J., Treu, T., Smith, G. P., & Ellis, R. S. 2004, *ApJ*, 604, 88
- Schulze, A., & Gebhardt, K. 2011, *ApJ*, 729, 21
- Schwarzschild, M. 1979, *ApJ*, 232, 236
- Shapiro, K. L., Cappellari, M., de Zeeuw, T., et al. 2006, *MNRAS*, 370, 559
- Shen, J., & Gebhardt, K. 2010, *ApJ*, 711, 484
- Siopis, C., Gebhardt, K., Lauer, T. R., et al. 2009, *ApJ*, 693, 946
- Spiniello, C., Koopmans, L. V. E., Trager, S. C., Czoske, O., & Treu, T. 2011, *MNRAS*, 417, 3000
- Teyssier, R., Moore, B., Martizzi, D., Dubois, Y., & Mayer, L. 2011, *MNRAS*, 414, 195
- Thomas, D., Maraston, C., & Bender, R. 2003, *MNRAS*, 339, 897
- Thomas, J., Ma, C.-P., McConnell, N. J., et al. 2016, *Nature*, 532, 340
- Thomas, J., Saglia, R. P., Bender, R., Erwin, P., & Fabricius, M. 2014, *ApJ*, 782, 39
- Thomas, J., Saglia, R. P., Bender, R., et al. 2004, *MNRAS*, 353, 391
- . 2011, *MNRAS*, 415, 545
- Tortora, C., Napolitano, N. R., Saglia, R. P., et al. 2014, *MNRAS*, 445, 162
- Treu, T., Auger, M. W., Koopmans, L. V. E., et al. 2010, *ApJ*, 709, 1195
- Trujillo, I., Erwin, P., Asensio Ramos, A., & Graham, A. W. 2004, *AJ*, 127, 1917
- van den Bosch, R. C. E., & de Zeeuw, P. T. 2010, *MNRAS*, 401, 1770
- Veale, M., Ma, C.-P., Greene, J. E., et al. 2018, *MNRAS*, 473, 5446
- Veale, M., Ma, C.-P., Thomas, J., et al. 2017, *MNRAS*, 464, 356
- Verolme, E. K., Cappellari, M., Copin, Y., et al. 2002, *MNRAS*, 335, 517
- Volonteri, M., Haardt, F., & Madau, P. 2003, *ApJ*, 582, 559
- Walsh, J. L., van den Bosch, R. C. E., Gebhardt, K., et al. 2015, *ApJ*, 808, 183
- Zhao, H. 1996, *MNRAS*, 278, 488